



Deposited via The University of Sheffield.

White Rose Research Online URL for this paper:

<https://eprints.whiterose.ac.uk/id/eprint/128042/>

Version: Accepted Version

Article:

Massey, C, Petley, D.N., Townsend, D. et al. (2018) Landslides Triggered by the MW 7.8 14 November 2016 Kaikoura Earthquake, New Zealand. Bulletin of the Seismological Society of America, 108 (3B). ISSN: 0037-1106

<https://doi.org/10.1785/0120170305>

Reuse

Items deposited in White Rose Research Online are protected by copyright, with all rights reserved unless indicated otherwise. They may be downloaded and/or printed for private study, or other acts as permitted by national copyright laws. The publisher or other rights holders may allow further reproduction and re-use of the full text version. This is indicated by the licence information on the White Rose Research Online record for the item.

Takedown

If you consider content in White Rose Research Online to be in breach of UK law, please notify us by emailing eprints@whiterose.ac.uk including the URL of the record and the reason for the withdrawal request.

1 **Landslides Triggered by the Mw 7.8 14 November 2016 Kaikoura Earthquake, New**
2 **Zealand**

3 C. Massey¹; D. Townsend¹; E. Rathje²; K.E. Allstadt³; B. Lukovic¹; Y. Kaneko¹; B. Bradley⁴; J.
4 Wartman⁵; R.W. Jibson³; D.N. Petley⁶; N. Horspool¹; I. Hamling¹; J. Carey¹; S. Cox¹; J.
5 Davidson⁴; S. Dellow¹; J.W. Godt³; C. Holden¹; K. Jones¹; A. Kaiser¹; M. Little²; B. Lyndsell¹;
6 S. McColl⁷; R. Morgenstern¹; F.K. Rengers³; D. Rhoades¹; B. Rosser¹; D. Strong¹; C. Singeisen¹;
7 M. Villeneuve⁴.

8 ¹ GNS Science, PO Box 30-368, Lower Hutt 5040, New Zealand; ² University of Texas, 110
9 Inner Campus Drive, Austin, TX 78705, USA; ³ U.S. Geological Survey, Box 25046, DFC, MS
10 966 Denver, CO 80225-0046, USA; ⁴ University of Canterbury, Private Bag 4800, Christchurch
11 8140, New Zealand; ⁵ University of Washington, 1410 NE Campus Parkway, Box 355852,
12 Seattle, WA 98195-5852, USA; ⁶University of Sheffield, Western Bank, Sheffield S10 2TN,
13 UK; and ⁷Massey University, Private Bag 11 222, Palmerston North 4442, New Zealand.

14
15
16
17
18
19
20
21
22
23

24 **Abstract**

25 The M_w 7.8 14 November 2016 Kaikoura earthquake generated more than 10000 landslides over
26 a total area of about 10000 km², with the majority concentrated in a smaller area of about 3600
27 km². The largest landslide triggered by the earthquake had an approximate volume of 20 (\pm 2) M
28 m³, with a runout distance of about 2.7 km, forming a dam on the Hapuku River. In this paper,
29 we present version 1.0 of the landslide inventory we have created for this event. We use the
30 inventory presented in this paper to identify and discuss some of the controls on the spatial
31 distribution of landslides triggered by the Kaikoura earthquake. Our main findings are (1) the
32 number of medium to large landslides (source area \geq 10000 m²) triggered by the Kaikoura
33 earthquake is smaller than for similar sized landslides triggered by similar magnitude
34 earthquakes in New Zealand; (2) seven of the largest eight landslides (from 5 to 20 x 10⁶ m³)
35 occurred on faults that ruptured to the surface during the earthquake; (3) the average landslide
36 density within 200 m of a mapped surface fault rupture is three times that at a distance of 2500 m
37 or more from a mapped surface fault rupture ; (4) the “distance to fault” predictor variable, when
38 used as a proxy for ground-motion intensity, and when combined with slope angle, geology and
39 elevation variables, has more power in predicting landslide probability than the modelled peak
40 ground acceleration or peak ground velocity; and (5) for the same slope angles, the coastal slopes
41 have landslide point densities that are an order of magnitude greater than those in similar
42 materials on the inland slopes, but their source areas are significantly smaller.

43 **Introduction**

44 The M_w 7.8 14 November 2016 Kaikoura earthquake in New Zealand occurred at 12:03 am local
45 time (Kaiser et al. 2017). The epicentre was located about 4 km from the rural town of Waiiau
46 (population 250) in North Canterbury (Figure 1), with rupture initiation at a shallow depth of

47 14.1 km (Nicol et al., this issue). Large, shallow earthquakes in mountain chains typically trigger
48 substantial numbers of landslides (Hovius et al., 1997; Parker, 2013; Hancox et al., 2014; 2016;
49 Xu et al., 2016). The Kaikoura earthquake (Dellow et al., 2017) triggered more than 10000
50 landslides over an area of about 10000 km², with the majority being focused in an area of about
51 3600 km² (Figure 1). Fortunately, the area affected by landslides is comparatively remote and
52 sparsely populated such that only a few dwellings were impacted by landslides, and there were
53 no recorded landslide-related fatalities (Stevenson, 2017). However, the landslides dammed
54 rivers, blocked roads and railways, and disrupted agricultural land throughout this region.
55 Landslides along the coast caused substantial damage to both State Highway (SH) 1 and the
56 northern section of the South Island Main Trunk Railway, blocking both in multiple locations
57 (Davies, 2017). At the time of writing, the section of SH1 north of Kaikoura is due to reopen on
58 15 December 2017, over a year after the earthquake.

59 The long-term stability of damaged but as yet unfailed slopes is a cause for concern in light of
60 the risk of future strong earthquakes and significant precipitation events. This has been
61 exemplified by debris flows and floods that occurred during rain associated with cyclones
62 Debbie (23 March to 7 April 2017) and Cook (14 April 2017), which caused several of the dams
63 to breach, releasing debris flows and floods that travelled several kilometres downstream. Debris
64 flows were also triggered on the steep coastal cliffs north and south of Kaikoura, leading to the
65 intermittent closures of the reopened portion of SH1 south of Kaikoura.

66 Both the number of landslides and the area affected are much less than expected based on
67 worldwide observations for an earthquake of this magnitude (Keefer, 2002; Malamud et al.
68 2004). To investigate the reason for this, we analyse an inventory we are creating of landslides
69 triggered by this earthquake; our analysis relates the spatial distribution and size characteristics

70 of the triggered landslides to geology, topography, strong shaking, and other geologic factors.
71 The objective of this paper is to describe these characteristics of the triggered landslides and
72 quantify their relationship to the various causative factors.

73 A broad-based investigation of the triggered landslides began immediately following the
74 earthquake. Dellow et al. (2017) provide a preliminary description of the landslides triggered by
75 this earthquake and the immediate response to document them and evaluate related hazards.
76 Jibson et al. (2017) give an overview of landslide types and distribution accompanied by
77 illustrations of the triggered landslides. In this paper, we present version 1.0 of the landslide
78 inventory we have created for this event, which builds on the earlier preliminary inventories
79 presented by Rathje et al. (2016) and Dellow et al. (2017). Refer to the Data and Resources
80 section of this paper for instructions about how to access this dataset. We present these findings
81 as a preliminary account of the potential controls we have observed on the landslide distribution
82 triggered by this event. It is version 1.0, because mapping is ongoing in those areas where the
83 landslide distribution was initially mapped from satellite images. The high-resolution
84 orthorectified aerial photographs that have been used to map much of the distribution were not
85 available in these areas at the time of publication.

86 **Detailed Landslide Inventory from Mapping**

87 Previous studies of worldwide earthquakes have related earthquake magnitude to the number of
88 landslides. For a M_w 7.8 earthquake, the relationship of Malamud et al. (2004) predicts about
89 25000 landslides; Keefer's (2002) relation predicts about 60000 landslides. Both relations are
90 based solely on magnitude and do not consider other factors such as earthquake depth, distance
91 to fault, topography, rock type, climate, and vegetation that contribute to landslide occurrence.

92 These estimates based on worldwide earthquakes are two to six times higher than the
93 approximate 10000 landslides mapped thus far from the Kaikoura earthquake.

94 The Version 1.0 landslide inventory contains 10195 coseismic landslides (Figures 1 and 2).
95 These landslides are inferred to have been triggered by the Kaikoura earthquake and associated
96 aftershocks as no major rain events occurred in the period between the earthquake and the first
97 low-level aerial photograph survey after the earthquake, dated December 2016, used to map the
98 distribution.

99 To map the distribution, we have primarily used post-earthquake 0.3 m ground resolution
100 orthorectified air photographs, and digital surface models derived from them, alongside digital
101 elevation models from post-earthquake airborne Light Detection and Ranging (lidar) surveys,
102 and other pre- and post- Kaikoura earthquake imagery and lidar data (these data sets are
103 described in Table A1). Landslides were manually digitised directly into a GIS. This was done
104 because the outputs from the automated landslide detection tools we ran generally performed
105 poorly. They: 1) wrongly identified areas of high albedo (in the images) as landslide sources e.g.,
106 identified bare farmland; 2) created multiple landslide source regions for individual landslide
107 sources and vice versa where large sources were in fact multiple individual landslides; and 3)
108 required significant time to manually edit. Several authors have shown how landslide mapping
109 can influence an inventory and therefore the results of any analyses of it. For example, Parker et
110 al. (2011) report more than 56000 landslides for the M_w 7.9 2008 Wenchuan earthquake, China,
111 but Xu et al. (2014; 2016) report 196007 mapped landslides and Li et al. (2014) report 57150
112 landslides. Li et al. (2014) attribute their increase in numbers over Parker et al. (2011) to them
113 separating individual landslides from amalgamated clusters. This change increased the number of
114 mapped landslides but decreased the total volume reported, e.g., see Li et al. (2014). Because of

115 such issues, we did not use the results of any of the automated landslide-detection algorithms.
116 Low-level orthorectified aerial photographs taken in 2015, before the earthquake, were used to
117 identify the many pre-earthquake landslides in the region, to ensure that such landslides were not
118 attributed to the earthquake. We also relied on the geotagged oblique air photos taken from
119 multiple post-earthquake helicopter reconnaissance missions to support and verify mapping in
120 areas of complex terrain. The landslide mapping was carried out by experienced landslide
121 researchers using the scheme outlined by Dellow et al. (2017). Where possible, we have
122 separated the landslide source area from the debris trail to allow more accurate estimates of
123 landslide size. This was done using a combination of aerial images, pre-and post-earthquake
124 ground surface difference models derived from lidar and photogrammetry, and shade models
125 generated from them, which helped to define landslide morphology. We used the scheme of
126 Hungr et al. (2014) to classify the landslides by their mechanism and dominant material type. To
127 date, the smallest mapped landslide source area is about 5 m² and the largest about 550,000 m².
128 Refinement of the inventory, in particular at the lower end of the size range, is ongoing. The
129 number of mapped landslides (frequency) with source areas of a given size has been binned
130 using source area bin widths that are equal in logarithmic space (Figure 2a). As expected, the
131 areas of the landslide sources generated by this event exhibit characteristic power-law scaling
132 (Figure 2b) (e.g., Hovius et al., 1997; Guzetti et al., 2002; Malamud et al., 2004; Parker et al.,
133 2015), defined by:

$$134 \quad p(A_L) = \frac{1}{N_{LT}} \cdot \frac{\delta N_L}{\delta A_L} \quad (1)$$

135 where $p(A_L)$ is the probability density of a given area within a near complete inventory—defined
136 as the frequency density of landslides of a given source area bin (A_L), divided by the total

137 number of landslides in the inventory— N_{LT} is the total number of landslides in the inventory, and
138 δN_L is the number of landslides with areas between A_L and $A_L + \delta A_L$. For the landslide area bins,
139 we adopted bin widths (δA_L) that increased with increasing landslide source area (A_L), so that bin
140 widths were equal in logarithmic space. The position of the characteristic rollover (Figure 2b),
141 for smaller landslides occurs at a landslide source area of about 50-100 m². The frequency-area
142 distributions of most landslide inventories exhibit a rollover at smaller landslide sizes for various
143 reasons, one of which is mapping resolution (Stark and Hovius, 2001).

144 The power-law scaling exponent (α) of 1.88, fitted to the Kaikoura landslide distribution using
145 the method of Clauset et al. (2009), with $x_{\min} = 500$ m², falls within the range of previously
146 observed values of landslide inventories (1.4 to 3.4), but it is below the central tendency of 2.3 to
147 2.5 (Van Den Eeckhaut et al., 2007; Stark and Guzzetti, 2009). Figure 2 shows the landslide
148 frequency and probability density versus area distributions for comparable inventories of
149 landslides triggered by other notable earthquakes in New Zealand. These are: 1) the 1929 M_W 7.8
150 Murchison earthquake (Hancox et al., 2016), where $N_{LT} = 6104$, $x_{\min} = 10000$ m² and $\alpha = 2.62$;
151 and 2) the 1968 M_W 7.1 Inangahua earthquake (Hancox et al., 2014), where $N_{LT} = 1199$, $x_{\min} =$
152 10000 m² and $\alpha = 2.71$.

153 Our results suggest that the number of large landslides >10000 m² generated by this earthquake
154 are less than those generated by the similar magnitude M_W 7.8 1929 Murchison earthquake in
155 New Zealand, but are instead more comparable to those triggered by the smaller magnitude M_W
156 7.1 1968 Inangahua, New Zealand earthquake. (Figure 2a). Nevertheless, the lower α -value
157 suggests that a higher number of larger landslides were triggered than would typically be
158 expected given the number of smaller landslides. Such comparisons, however, do not consider
159 differences in the physiographic setting, which could affect the numbers of landslides generated.

160 Although a more detailed comparison of the landslides from these different earthquakes is
161 warranted, it is currently outside the scope of this paper.

162 **The Geology and Topography of the Study Area**

163 The region in which most of the landslides occurred can be subdivided into four main geological
164 units (Figure 1b and Table 1). These are described by Rattenbury et al. (2006), and their
165 descriptions are summarised here in order of oldest to youngest: 1) Lower Cretaceous Torlesse
166 (Pahau terrane) “basement” rocks formed primarily of greywacke; 2) Upper Cretaceous and
167 Paleogene limestones, siltstones, conglomerates and minor volcanic rocks; 3) Neogene
168 limestones, sandstones and siltstones; and 4) Quaternary sands, silts and gravels. These materials
169 and their properties tend to control the types of landslides that occurred within them. For
170 example, the greywacke is highly jointed, and most landslides appear to be debris avalanches,
171 controlled by multiple intersecting joint blocks, which limit the volume of such failures.
172 Conversely the Upper Cretaceous and Neogene sandstones and siltstone tend to be massive with
173 highly persistent bedding planes and clay seams, which allow the development of large
174 translational debris slides and slumps. These relationships are explained further in Table 1.

175 The earthquake mainly affected the northeastern portion of New Zealand’s South Island. This
176 area is dominated by the Kaikoura Ranges, which rise from sea level to a maximum elevation of
177 2885 m above mean sea level (AMSL) at Mount Tapuae-o-Uenuku. The Kaikoura Ranges are
178 predominantly formed of greywacke and are dissected by several large rivers. The long, straight
179 Clarence River valley separates the Seaward Kaikoura Ranges from the longer and steeper
180 Inland Kaikoura Ranges, including Mount Tapuae-o-Uenuku. Beyond the Inland Kaikoura
181 Range is the valley of the Awatere River, which runs parallel to that of the Clarence River. As
182 these rivers approach the coast, the slopes reduce in gradient, where they are predominantly

183 formed of faulted slivers of Neogene rocks and Quaternary gravel, sand and silt. The township of
184 Kaikoura is the largest town in the area and is located on a rocky peninsula formed of Cretaceous
185 to Neogene sedimentary rocks and Quaternary marine terraces, about 70 km northeast of the
186 earthquake epicentre (Figure 1). The topography south and west of Kaikoura is relatively gentle
187 compared to the Inland and Seaward Kaikoura Ranges. The slopes have mainly been formed by
188 tectonically driven uplift and fluvial incision through the Neogene sandstones and siltstones,
189 which forms the main bedrock unit in the area. The climate across much of the area is temperate
190 and it typically experiences dry, cold winters..

191 **Controls on the Spatial Distribution of Landslides**

192 The landslide distribution does not represent a homogenous mass of landslides clustered around
193 the earthquake epicentre. Instead, the mapped distribution shows a long, generally linear pattern,
194 with many landslides occurring on either side of the faults that ruptured to the ground surface
195 (Figure 1), to the northeast of the earthquake epicentre. Many smaller landslides concentrate
196 along the coast and in discrete clusters on either side of the faults that ruptured. Many of the
197 larger landslides occurred on faults with surface ruptures that passed through their source areas
198 (Figure 3). Interestingly, the larger landslides, whilst also occurring in clusters along the faults,
199 do not appear to occur at the same locations as the clusters of smaller landslides. A comparison
200 of the mapped distribution with the bedrock geology shows that landslide occurrence is a
201 function of lithological variations across the area, and field observations suggest that such
202 variations control the nature and type of landslides triggered by the earthquake (Figure 1b, Table
203 1). For example, the landslide point density in the massive, but weaker Neogene sandstones and
204 siltstones is 5.5 landslides km⁻², compared to 2.5 landslides km⁻² in the stronger but closely
205 jointed greywacke (Table 1).

206 The dynamic response of a slope during an earthquake is not controlled solely by lithology but
207 comprises a complex interaction between seismic waves and the hillslope (e.g., Ashford et al.,
208 1997; Sepulveda et al., 2005; 2011; Massey et al., 2016; Rai et al., 2016). We have used our
209 mapped landslide distribution to explore the relationships between the occurrence of a landslide
210 and the variables that may control its occurrence (Table 2), which we have broadly grouped into:
211 1) predominantly landslide forcing variables representing the intensity of the event-specific
212 seismic ground motions and their proxies, for the Kaikoura earthquake; and 2) predominantly
213 landslide susceptibility variables that capture the strength of the hillslope materials at a regional
214 scale and the static shear stresses at the slope scale.

215 We used logistic regression (e.g., Von Ruetten et al., 2011; Parker et al., 2015) to investigate the
216 influence that the variables listed in Table 2 have on the spatial distribution of coseismic
217 landslides attributed to the Kaikoura earthquake. The method models the influence of multiple
218 predictor variables on a categorical response variable Y (with possible values 0 or 1) using:

$$219 \quad P_{LS}(Y = 1) = \frac{1}{1 + \exp(-(b_0 + b_1x_1 + b_2x_2 + b_3x_3 \dots b_nx_n))} \quad (2)$$

220 where logistic regression is used to estimate the coefficients $(b, b_n \dots)$ for predicting the
221 probability (P_{LS}) that $Y = 1$, given the values of one or more predictor variables $(x, x_n \dots)$. The
222 condition $Y = 1$ corresponds to the occurrence of a landslide within a sample grid cell. The
223 regression coefficients are estimated using a maximum likelihood criterion.

224 To undertake logistic regression, we have defined a sample grid at 32 m resolution, based upon
225 an 8 m ground resolution digital elevation model, resampled from the 2012 version of the Land
226 Information New Zealand (LINZ) digital elevation model for New Zealand. The 32 m grid mesh
227 is much less than the typical hillslope lengths in the region, which can vary from 100 to $\gg 1000$

228 m. For this assessment, we have used only landslide source areas and not the debris trails.
229 Landslides with areas less than 50 m² were removed from our data set to eliminate sample bias,
230 because landslides smaller than this have not been systematically mapped and may be
231 underrepresented in the inventory. Thus we have assumed that $Y = 1$ for any given sample grid
232 cell in which its centroid falls within a landslide source area, even if the grid cell is not fully
233 occupied by a landslide source.

234 The predictor variables used in this assessment were chosen based on variables previously found
235 to influence landslide occurrence (listed in Table 2 and shown in Figures 1b, 4, 5 and 6a to d). To
236 represent the landslide forcing variables, we adopted: 1) peak ground velocity models (PGV); 2)
237 peak ground acceleration models (PGA); 3) the proximity of a landslide to a coseismic fault
238 rupture; 4) permanent coseismic “fault” displacement derived from InSAR and GPS
239 measurements (Hamling et al., 2017) (Figure 5); and 5) local slope relief (LSR). We adopted
240 variables 1) and 2) as proxies for ground shaking, and variables 3) and 4) as less direct proxies
241 for ground shaking. The permanent coseismic displacement variable also serves as a proxy for
242 other susceptibility factors such as rock mass damage and steeper and higher relief. This is
243 because displacement can lead to rock mass deformation and displacement in a vertical sense
244 (uplift) is usually associated with reverse fault hanging walls, which in the Kaikoura region are
245 where the steeper slopes are located. The proximity to a fault is inherently included in the
246 estimation of PGV and PGA; however, we included it separately to examine the influence of
247 local ground deformation and other near-field effects that might not be fully taken into account
248 in the ground-motion models. To include this in the model, we determined the horizontal
249 distance of each sample grid cell to the surface projection of the nearest fault that ruptured to the
250 surface. Note that these faults are different than the locations of the simplified faults used in the

251 Hamling et al. (2017) fault model, and its variations, which was used in the ground motion
252 modelling of PGA and PGV. It should also be noted that the proximity to fault variable does not
253 account for faults that did not rupture to the surface, but which also contribute to the shaking
254 intensity. The location of those faults that ruptured to the surface during the earthquake were
255 taken from the GNS Science Active Faults database (Langridge et al., 2016; Stirling et al., 2017;
256 Litchfield et al., this issue). Local slope relief (LSR) was defined as the maximum height
257 difference within a fixed 80 m radius of the centroid of a given grid cell. It represents a proxy for
258 slopes that could amplify ground shaking due to their “larger-scale relief” (larger than just a
259 sample grid cell-size), where larger values of LSR represent the steeper and higher slopes of the
260 region, which can amplify ground shaking more than lower-in-height and less steep slopes
261 (Ashford et al. 1997; Massey et al., 2016; Rai et al., 2016; see Table 2 for details). We also used
262 slope aspect to investigate directivity effects caused by the earthquake-rupture sequence on
263 landslide occurrence, refer to Table 2 for details.

264 To estimate the PGV and PGA variables, we have used three different ground motion models, as
265 follows: 1) $PGV_{BRADLEY}$ from Bradley et al. (2017); 2) PGV_{LF} , which is low-frequency (long
266 period) PGV calculated up to 0.33 Hz, and derived using the method described by Holden et al.
267 (2017); 3) PGA_{SM} and PGV_{SM} from ShakeMap NZ (listed in the Data and Resources section of
268 this paper), developed by the USGS (Wald et al., 1999; Worden et al., 2012), and calibrated for
269 New Zealand by Horspool et al. (2015) (Figure 4c and d). The first two models incorporate
270 directivity and basin amplification effects using 3D velocity models and account for along-strike
271 variations in fault slip, whereas the third does not directly account for any of those effects except
272 where they are captured by felt reports or seismic data. All three ground motions models are
273 based on the fault-source model of Hamling et al. (2017). All models use the strong motion data

274 for the earthquake recorded by the GeoNet strong motion stations located within the area
275 affected (Figures 1 and 4). However, there were only four stations within the 3600 km² main area
276 that was affected by landslides, about one station for every 900 km², and 13 in the wider area
277 affected (10000 km²), about one station for every 800 km². The minimum, maximum and mean
278 distance between these stations was 6.5, 51.3 and 23.6 km, respectively, indicating a sparse
279 coverage of stations for the main area affected by landslides.

280 We used landslide susceptibility variables of: 1) elevation; 2) slope curvature; and 3) geology.
281 Curvature was used as a proxy to represent potential slope-scale patterns of topographic
282 amplification that tend to occur at breaks in slope (Ashford et al., 1997; Rai et al. 2016) and
283 localised slope morphology that could represent pre-earthquake landslide scarps and therefore
284 potentially unstable slopes, thus representing both a susceptibility and earthquake forcing
285 variable. Curvature is scale dependent and will vary as a result of both the size of the landslide
286 and the slope. For this paper, curvature was calculated using ArcGIS and taken from the
287 curvature of the surface on a cell-by-cell basis, as fitted through that cell and its eight
288 surrounding neighbours. This appeared to best capture the more significant breaks in slope
289 relative to the scale of the morphology of the slopes along the coast and inland, but not the
290 higher peaks of the Kaikoura Ranges. Further work is needed to investigate the scale dependency
291 of slope curvature and its effects on landslide occurrence. Slope gradient and elevation of each
292 32 m sample grid cell were measured by taking the mean values from the n=16, 8 x 8 m grid
293 cells that fell within it. Table 2 details how these variables were calculated. We used a
294 categorical variable to represent the main geological units present in the area (Table 1 and
295 summarised in Table 2), adopting four categories.

296 Model fitting was done manually using the Statistica software (Statistica, 2017). For a predictor
 297 variable to be included in the model, it must have a logical and statistically significant influence
 298 on P_{LS} . We used a significance level (p-value) of $p < 0.05$ (using the Wald statistic) as the
 299 threshold for inclusion in the model. During model fitting, multiple variable combinations were
 300 iteratively tested. To ensure that the predictor variables included in the model do not exhibit
 301 multicollinearity, we used a variance inflation factor matrix (VIF), given as:

$$302 \quad VIF = \frac{1}{1-R^2} \quad (3)$$

303 where R^2 is the linear coefficient of determination of the relationship between any pair of
 304 predictor variables. Pairs with $VIF > 10$, indicating a high level of multicollinearity, are avoided
 305 in our models (Kutner et al., 2004; Parker et al., 2015), (Table A2). The final models represent
 306 those variables that produced the best fit whilst meeting the significance level and
 307 multicollinearity criteria.

308 **Results**

309 We independently derived two models—one adopting PGA_{SM} and one adopting PGV_{SM} as the
 310 ground motion parameter—to hindcast the probability of a landslide occurring in each grid cell.
 311 Landslide probability (P_{LS}) is given by the following equation for PGA:

$$312 \quad P_{LS} = \frac{1}{1 + \exp\left(-\left(\begin{array}{l} C_{Intercept} + C_{PGA_{SM}} \cdot PGA_{SM} + C_{FaultDist} \cdot FaultDist + C_{Elev_{MEAN}} \cdot Elev_{MEAN} \\ + C_{Slope_{MEAN}} \cdot Slope_{MEAN} + C_{LSR} \cdot LSR + C_{Geology_X} \end{array}\right)\right)} \quad (4)$$

313 where the regression coefficients are denoted by c . The regression coefficients and goodness of
 314 fit statistics are shown in Tables 3 and 4 for models adopting PGA_{SM} and PGV_{SM} as the ground
 315 motion predictor variables. We found that the best combination of predictor variables used to

316 estimate landslide probability were regional ground motion models (PGA_{SM} or PGV_{SM}), distance
317 to the surface expression of a fault that ruptured, slope gradient, elevation, local slope relief, and
318 geology. All the other variables tested during model fitting were found to be less effective
319 predictors than those included in the models, or they failed either the statistical significance test
320 ($p < 0.05$) or the variance inflation factor test.

321 Figures 6E and 6F show the spatial distribution of P_{LS} calculated using the two regression
322 models (Tables 3 and 4). The only difference between the combinations of variables used in each
323 model is the ground motion parameter (PGA_{SM} and PGV_{SM}). The results show that there is little
324 statistical (Tables 3 and 4) or spatial (Figures 6e and f) difference between the model outputs of
325 P_{LS} . There was also little difference in the modelled P_{LS} , when substituting other ground motion
326 variables ($PGV_{BRADLEY}$, PGV_{LF} and PGV_{MEAN}) independently in the model, whilst keeping the
327 other variables fixed. To further investigate the explanatory power of the other variables on P_{LS} ,
328 we have adopted a model that uses PGV_{SM} (Table 4), because the model results have a
329 marginally higher coefficient of determination—pseudo R^2 adopting Nagelkerke's R^2 method—
330 than those when the other PGV or PGA ground motion variables were adopted. Although the
331 pseudo R^2 of this model is relatively low, it is comparable to other similar studies on landslide
332 data sets from New Zealand (Parker et al., 2015).

333 Although the predictive power of the model on P_{LS} is low, it has no apparent biases in any part of
334 its range. Figure 7 presents a comparison of observed versus predicted P_{LS} . This relationship was
335 calculated by accumulating (adding) the predicted P_{LS} values for each sample grid cell from
336 smallest to largest, along with the corresponding observed Y value for the same grid cell. For the
337 PGA_{SM} and PGV_{SM} models, the observed and predicted probabilities display a good fit to the line
338 of equality. This shows that the modelled probabilities are broadly consistent with the data. The

339 low pseudo R^2 of the model indicates that there are many landslides in cells with low values of
340 P_{LS} . For example, the model adopting PGV_{SM} has about 43100 cells that are classified as being
341 landslides ($Y = 1$) where the modelled landslide probability is $\leq 10\%$. However, there are over
342 3.4M cells where the modelled probability of a landslide occurring is less than 10%, resulting in
343 a landslide pixel density of about 0.005 landslides per cell. Conversely, there are only 228 pixels
344 where the modelled landslide probability is $> 50\%$, of which 26 are classified as being landslides,
345 resulting in a landslide pixel density of 0.11.

346 Figure 8 shows the predictor variables in rank order of significance, which we determined by
347 sequentially removing each of the predictor variables that contribute least to the fit of the models.
348 In each model, and in order of importance, the slope angle, distance to fault, elevation and
349 geology variables contribute most to the fit of the models, followed by PGV_{SM} (or PGA_{SM} when
350 substituted for PGV_{SM} in the model) and local slope relief. Notably, distance to the surface
351 expression of a fault that ruptured has more explanatory power in the regression model than
352 PGA_{SM} or PGV_{SM} ground motion models or any of the other modelled PGV variables when
353 tested independently within the regression model. This variable may be capturing: 1) additional
354 ground motion parameters such as high-frequency ground motions that are not captured by the
355 current PGA and PGV models, but which will sharply decay with distance from a fault; 2) the
356 complex nature of the multi-fault rupture, and the multi-frequency ground motion intensity—and
357 not just the higher frequency ground motions—better than the current PGA and PGV models
358 even though it doesn't take into account the shaking contributed by those faults that did not
359 rupture to the surface; and 3) the influence of rock mass damage on the rock mass strength,
360 where rock masses closer to faults are likely to be more jointed or “damaged” and have lower
361 mass strengths than those less damaged rock masses, formed in similar materials, located farther

362 away from faults. In addition, preexisting persistent discontinuities such as faults and permanent
363 tectonic surface deformation along some of them could have been important in triggering several
364 of the large landslides located directly on or close to faults that ruptured to the surface.

365 The relatively low pseudo R^2 value of the model might be taken to suggest that variables not
366 considered in the presented models might be important for predicting P_{LS} . For example, only four
367 main geological units have been adopted even though there are significant differences in rock
368 type and their associated physical properties within these four broad groups. Such differences in
369 their properties have not yet been determined in sufficient detail to be included in the models.
370 Also, the northwestern part of the main area affected by landslides contains a cluster of many
371 small landslides (west-southwest of Ward, Figure 1), situated in areas of Neogene mudstone.
372 This area does not “stand out” in the models as having a high P_{LS} , and ground shaking (Figure 4)
373 was relatively low in this area during the Kaikoura earthquake with no nearby faults rupturing,
374 which suggests that some other variable may be needed to explain this distribution. This area was
375 affected by the M_w 6.5 16 August 2013 Lake Grassmere earthquake, and to a lesser extent by the
376 M_w 6.6 21 July 2013 Cook Strait earthquake (Figure 1) (Van Dissen et al. 2013). The Lake
377 Grassmere earthquake generated landslides in this area, and it induced slope cracking. Thus, the
378 Lake Grassmere earthquake may have preconditioned the slopes in the area to fail in the
379 subsequent Kaikoura earthquake (as described by Parker et al., 2015). Alternatively, the
380 mismatch between modelled and observed landsliding could be due to the high amplitude of the
381 shaking in this area from the large amount of slip on the Kekerengu fault (Litchfield et al., this
382 issue), which may not be captured by the current ground motion models.

383 **Discussion**

384 **Kaikoura earthquake landslide numbers and their size**

385 Our results suggest that the number of large landslides $>10000 \text{ m}^2$ generated by this earthquake
386 is fewer than the number generated by the similar magnitude $M_w 7.8$ 1929 Murchison earthquake
387 in New Zealand and similar to the number triggered by the smaller magnitude $M_w 7.1$ 1968
388 Inangahua earthquake. One reason for this might be that the area affected by strong shaking and
389 landslides is topographically constrained. Specifically, several of the faults that ruptured to the
390 surface extended off shore, leading to the triggering of many submarine landslides (Mountjoy et
391 al., this issue), which are not taken into account in the terrestrial landslide distribution examined
392 in this paper. Another reason for this difference may be that the Kaikoura earthquake involved
393 the rupture of more than 20 faults that broke to the land surface over a fault-zone length of more
394 than 100 km, suggesting that the earthquake comprised numerous “sub-events” (Kaiser et al.,
395 2017; Stirling et al., 2017) of lower magnitude (Hamling et al., 2017). For each fault that
396 ruptured, an equivalent magnitude can be calculated based on fault dimensions and estimated
397 total slip (estimated either from geodetic and/or seismic data inversion). Hamling et al. (2017)
398 estimated that the cumulative moment from the faults that ruptured south of Kaikoura equates to
399 a $M_w 7.5$ earthquake. Even though the cumulative moment from the northern faults is larger than
400 from the southern faults, the moment from some of the individual smaller faults that ruptured to
401 the north of Kaikoura was equivalent to a $M_w 7.1$ earthquake (Hamling et al. 2017). This would
402 conceptually result in the shaking energy being distributed over a larger area but at a smaller
403 amplitude and, possibly, duration. Large landslides are possibly more sensitive to shaking in the
404 range of frequencies that often control the ground motion PGV. If the moment release was
405 distributed across many faults, the shaking duration and frequency content would reflect rupture

406 from many smaller faults rather than a single large fault. Thus, the shaking would not have the
407 same intensity as would be produced by a single fault rupturing with M_w 7.8. With this in mind,
408 it will be important to update the landslide regression models as improved ground motion
409 modelling for the earthquake becomes available.

410 **Possible controls on the size of the landslides triggered by the earthquake:**

411 The strength of the dominant rock type in the area that was strongly shaken was mainly
412 greywacke, and it accounts for 60% of the rocks in the main area affected by landslides. The
413 coseismic landslide distribution in greywacke is dominated by many small landslides with few
414 very large ones. Non-earthquake induced landslides in such materials have in the past been
415 limited in size as greywacke tends to be highly jointed, favouring smaller failures (Hancox et al.,
416 2015). Previous work on fracture spacing in Torlesse Schist of the Southern Alps, suggests that
417 its properties are highly influential in geomorphic response (Hales and Roering, 2009).

418 Additional work is required to assess the landslide distribution source areas and volumes with
419 regards to the main geological materials in which they occurred, and the role of rock mass
420 conditioning of landslide source areas/volumes. Such an assessment is outside the scope of this
421 current paper.

422 Another contributing factor might be that high-frequency energy radiation during the Kaikoura
423 earthquake is inferred by some researchers as smaller than during other landslide-triggering
424 crustal earthquakes of a similar magnitude. While the energy magnitude (M_e) of the Kaikoura
425 and M_w 7.8 2008 Wenchuan, China earthquakes derived from low-frequency (0.5 – 70 s)
426 waveforms (IRIS DMC, 2013a) are similar ($M_e = 7.93$ and 8.06, respectively), there is a
427 significant difference in the energy magnitudes estimated from higher frequency (0.5 – 2 s)
428 waveforms ($M_e = 7.59$ and 8.05, respectively) (IRIS DMC, 2013b).

429 **The role of distance from the surface fault rupture**

430 To explore the relationship between landslide occurrence and proximity to a surface fault
431 rupture, we have plotted the landslide point and area densities as a function of the distance from
432 the surface expression of the nearest fault that ruptured (Figure 9). We did this by creating
433 successive buffer zones around the mapped fault traces that ruptured to the surface (Litchfield et
434 al., this issue; Nicol et al., this issue). We then computed the number and total area of landslide
435 source areas within each successive 200 m buffer to a distance of 3000 m on either side of the
436 mapped fault trace as well as those landslide source areas through which faults pass. The density
437 of landsliding in areas outside the fault buffers was also calculated for comparison. The results
438 show that the landslide densities (both point and area) within 200 m of a fault are as much as
439 three times greater than densities outside the 3000 m buffers. The results also show a general
440 decrease in landslide density with increasing distance from a fault. At a distance of about 2500 to
441 3000 m, the background landslide density (termed “rest of area” in Figure 9) is reached. This
442 finding may be the result of: a) high-frequency shaking, which declines rapidly with distance
443 from a fault, being an important control on the density of landslides triggered by the Kaikoura
444 earthquake; b) the rock masses close to faults being weaker because of damage from previous
445 fault rupture events; and c) slopes nearer faults often exhibit greater relief and are steeper than
446 those farther away, which is the case for those slopes in the Kaikoura region. Others have
447 reported similar findings, for example, Scheingrosset al. (2013) hypothesized that earthflows
448 tend to cluster near the creeping San Andreas Fault because of a fault-induced zone of reduced
449 bulk-rock strength that increases hillslope susceptibility to failure. Meunier et al. (2007) also
450 suggested that near-field (near-fault), high-frequency shaking is likely to have been an important
451 control on the density of landslides triggered by earthquakes.

452 Only 44 of the mapped landslide source areas are directly intersected by faults that ruptured to
453 the surface, but this number includes seven of the eight largest landslides triggered by the
454 Kaikoura earthquake. This would suggest that the initiation of these large landslides might have
455 been due to a combination of preexisting discontinuities such as faults and rock mass damage,
456 dynamic strong shaking and permanent tectonic displacement of the fault as it ruptured to the
457 surface within the source area.

458 **Earthquake ground motion frequency, slope amplification and landsliding**

459 As noted above, our logistic regression analysis indicates that PGA (or PGV when substituted for
460 PGA in the model) from the ShakeMap NZ models performs best, but overall the PGA (or PGV)
461 variable has low explanatory power on predicting landslide occurrence. Distance to fault, which
462 may capture additional ground motion parameters, has a much higher explanatory power.

463 Generally, the shaking nearer the source contains a lot more high-frequency energy than farther
464 away (e.g., Davies, 2015), suggesting that ground motion frequency may play a key role in
465 determining slope response. Therefore, slopes that are near faults that rupture are more likely to
466 experience such high-frequency ground motions. If the fundamental frequency of the slope is
467 similar to the dominant frequency of the ground motion, amplification of shaking may also occur
468 (Geli et al., 1988).

469 Ashford et al. (1997) showed that the fundamental frequency (f) of a slope behind the crest can
470 be estimated using the following equation:

$$471 \quad f = \frac{4 \times H}{v_s} \quad (5a)$$

472 and a slope/topographic frequency:

473 $f = \frac{5 \times H}{V_s}$ (5b)

474 where H is the slope height (or relief) and V_s is the shear wave velocity of the material forming
475 the slope. More recently, Rai et al. (2016) have developed a model to predict the effects of
476 topography on earthquake ground motions, adopting the relative relief of a slope (like the LSR
477 used in this paper). For slopes in the main area affected by landslides, the mean and modal
478 values for slope relief are 135 m and 85 m for coastal slopes, and for inland slopes they are 588
479 m and 103 m, respectively. The mean V_{s30} of the rock forming the coastal and inland slopes is
480 estimated by Perrin et al. (2015) as 1000 m/s. Equation (5a) yields fundamental frequencies of
481 the coastal slopes ranging from 1.9 to 2.9 Hz, and of the inland slopes from 0.4 to 2.4 Hz, for the
482 mean and modal slope relief, respectively. Such fundamental frequencies are relatively high,
483 suggesting that the combination of high-frequency shaking at close proximity to the faults, and
484 amplification of shaking caused by the slopes responding to such high-frequency shaking, may
485 explain why so many landslides occurred on slopes adjacent to faults. It should be noted that it is
486 not just the fundamental frequency of the hillslope that matters, which will scale with slope
487 morphology and relief, but also the fundamental frequency of the potential failure mass, which is
488 likely to be shallower, and therefore have a higher fundamental frequency than the overall slope.
489 However, such a difference may only be distinguishable from the rest of the slope if there is
490 some preexisting plane or damage resulting in a contrast of density/shear wave velocity between
491 the potential failure mass and the slope (e.g., Massey et al., 2016).

492 **Landslide slope angle and elevation**

493 We have explored the higher density of landslides on the coastal slopes by attributing the
494 centroid of each landslide source area with its mean slope angle and elevation. We split the

495 landslide distribution into coastal and non-coastal slopes—where coastal slopes are defined as
496 those that extend from the sea to the first main inland ridge line, an approximate strip about 1 km
497 wide—and calculated the area of coastal/non-coastal slope within each slope angle bin (Figure
498 10). The results show that coastal slopes consistently have more landslides for a given slope
499 angle than corresponding inland slopes, but that the mean size of the landslide sources on the
500 inland slopes is larger than those on coastal slopes. Variations in slope angle and geology cannot
501 explain this difference because the proportion of inland slopes in the steeper slope angle bins
502 (Figure 10b, inset) is larger than the proportion of slopes on the coast within the same
503 corresponding slope angle bins. The coastal slopes are primarily formed from greywacke, which
504 is also the dominant rock type forming the slopes inland. A possible explanation for these
505 smaller landslides on the coastal slopes is that their size has been limited by the topography, as
506 the coastal slopes have a lower relief (i.e., elevations less than 500 m AMSL) compared to the
507 higher relief slopes inland.

508 The results of the logistic regression model show that landslide probability increases with
509 decreasing elevation and coastal slopes are at lower elevations. This finding could be due to the
510 coastal-slope geometry and materials (and contrasting materials caused by coastal weathering
511 processes and products), and their effects on amplifying the ground shaking. Studies of similar
512 coastal slopes (Massey et al., 2016), albeit in different materials, have shown that
513 amplification—between the peak acceleration of the free field earthquake motion and the
514 average peak acceleration of the slope—of shaking between the base and crest of a slope could
515 be up to 2.5 times, with a mean of 1.6 times, higher at the crest than the base of the slope. Such
516 values are comparable to the amplification factors reported by Ashford et al. (1997). It is also
517 possible that the predominantly greywacke coastal slopes are more weathered than their inland

518 counterparts. Such hypotheses are likely to form the basis of future research on the landslides
519 generated by the Kaikoura earthquake.

520 **Conclusions**

521 Our main findings are: (1) the number of large landslides (with source areas $\geq 10000 \text{ m}^2$)
522 triggered by the Kaikoura earthquake is fewer than the number of similar sized landslides
523 triggered by other similar magnitude earthquakes in New Zealand; (2) the largest landslides
524 (with source volumes from 5 to 20 M m^3) occurred either on or within 2500 m of the more than
525 20 mapped faults that ruptured to the surface; (3) the landslide density within 200 m of a mapped
526 surface fault rupture is as much as three times higher than those densities farther than 2500 m
527 from a ruptured fault; (4) for the same slope angles, coastal slopes have landslide point densities
528 that are an order of magnitude greater than those in similar materials on the inland slopes, but
529 their source areas are significantly smaller, possibly indicating that these slopes locally amplified
530 ground shaking, and (5) the “distance to fault” predictor variable, when used as a proxy for
531 ground motion intensity, has more explanatory power in predicting landslide probability than the
532 modelled PGA or PGV variables adopted in the logistic regression modelling, even though this
533 variable does not account for faults that did not rupture to the surface, but which also contribute
534 to the shaking intensity. This relationship might be because the distance to fault variable
535 captures: (a) the high-frequency ground motions and their attenuation with distance from a fault
536 better than the current PGA and PGV models; (b) the complexity of the multi-fault rupture, and
537 therefore the multi-frequency ground motion intensity, better than the current PGA and PGV
538 models; and (c) the more damaged nature of the rock masses close to the faults, where they tend
539 to be more sheared and weakened. The strong explanatory power of the “distance to fault”

540 predictor variable could also reflect the apparent structural control of some of the largest
541 landslides that occur on or near faults.

542 **Data and Resources**

543 A recent update on information relating to submarine landslides triggered by the Kaikoura
544 earthquake was given in the AGU Landslide Blog. 2017. Last accessed October 2017.

545 <http://blogs.agu.org/landslideblog/2017/02/27/niwa-1/>

546 The ShakeMap NZ map of peak ground accelerations for the Kaikoura earthquake was published
547 online on the GeoNet website. 2016. Last accessed October 2017.

548 <http://www.geonet.org.nz/news/fiBlIE2uNq2qGmmiOg42m>

549 The software package used to carry out the logistic regression is called Statistica. 2017. Last
550 accessed October 2017. <http://www.statsoft.com/Products/STATISTICA-Features>

551 The version 1.0 landslide dataset used in this paper can be downloaded from the GNS Science
552 landslide database <https://data.gns.cri.nz/landslides/> or the <https://www.designsafe-ci.org/>
553 website.

554 **Acknowledgements**

555 The GeoNet project, the New Zealand Natural Hazards Research Platform and GNS Science
556 Strategic Science Investment Fund (Landslide Hazards project) funded this work. The two
557 anonymous reviewers and Eric Thompson (U.S. Geological Survey) made some very
558 constructive and insightful comments. Nicola Litchfield and Russ Van Dissen (GNS Science)
559 reviewed drafts of this paper. We would also like to thank Nicholas Sitar (UC Berkeley, USA),
560 and Marin Clark and Dimitrios Zekkos (University of Michigan, USA), for the time they spent in

561 the field with the GNS Science landslide response team. Any use of trade, firm, or product
562 names is for descriptive purposes only and does not imply endorsement by the U.S. Government.

563 **References**

564 Ashford, S.A., Sitar, N., Lysmer, J., and N. Deng (1997) Topographic effects on the seismic
565 response of steep slopes. *Bull. Seism. Soc. Am.* **87** 701-709.

566 Bradley, B.A., Hoby, N., Razafindrakoto. T, and V. Polak (2017) Ground-motion observations
567 from the 14 November 2016 M_w 7.8 Kaikoura, New Zealand, earthquake and insights from
568 broadband simulations. 2017. *Seismological Research Letters.* **88** 1–17.

569 Clauset, A., Shalizi, C.R., and M.E.J. Newman (2009). Power-law distributions in empirical data.
570 *SIAM Review* **51**, 661-703. DOI: 10.1137/070710111.

571 Davies, A.J. (2017) Transport infrastructures performance and management in the South Island
572 of New Zealand during the first 100 days following the 2016 M_w 7.8 Kaikōura earthquake.
573 *Bulletin of the New Zealand Society for Earthquake Engineering, Kaikoura Earthquake Special*
574 *Issue.* **50** 271-298.

575 Davies, T. (2015). *Landslide hazards, risk and disasters.* Volume editor Tim Davies. Hazards and
576 disasters series. ISBN 978-0-12-396452-6. Elsevier, Amsterdam. 2015. Page 104.

577 Dellow, G.D.; Massey, C.I.; Cox, S.C.; Archibald, G.C.; Begg, J.G.; Bruce, Z.R.; Carey, J.M.;
578 Davidson, J.; Della-Pasqua, F.N.; Glassey, P., et al. (2017). Landslides caused by the M_w 7.8
579 Kaikoura earthquake and the immediate response. *Bulletin of the New Zealand Society for*
580 *Earthquake Engineering, Kaikoura Earthquake Special Issue.* **50** 106-116.

581 Geli, L., Bard, P.-Y., and B. Jullien (1988). The effect of topography on earthquake ground
582 motion: A review and new results. *Bull. Seism. Soc. Am.* **78** 42–63.

583 Guzzetti, F., Malamud, B. D., Turcotte, D. L., and P. Reichenbach (2002). Power-law
584 correlations of landslide areas in central Italy. *Earth and Planetary Science Letters*, **195** 169-183.

585 Hales, T.C., and J.J. Roering (2009). A frost “buzzsaw” mechanism for erosion of the eastern
586 Southern Alps, New Zealand. *Geomorphology* **107** 241–253.

587 Hamling, I., Hreinsdóttir, S., Clark, K., Elliott, J., Liang, C., Fielding, E., Litchfield, N.,
588 Villamore, P., Wallace, L., Wright, T.J., et al. (2017). Complex multifault rupture during the
589 2016 M_w 7.8 Kaikoura earthquake, New Zealand. *Science* **356** 1-16. DOI:
590 [10.1126/science.aam7194](https://doi.org/10.1126/science.aam7194)

591 Hancox, G.T., Ries, W.F, Lukovic, B., and R.N. Parker (2014). Landslides and ground damage
592 caused by the MW 7.1 Inangahua earthquake of 24 May 1968 in northwest South Island, New
593 Zealand. GNS Science Report 2014/06.

594 Hancox, G.T., Perrin, N.D., Lukovic, B., and C.I. Massey (2015). Quantifying the seismic
595 response of slopes in Christchurch and Wellington: Wellington slope types and characterisation.
596 GNS Science Report 2013/58.

597 Hancox, G.T., Ries, W.F, Parker, R.N., and B. Rosser (2016). Landslides caused by the M_w 7.8
598 Murchison earthquake of 17 June 1929 in northwest South Island, New Zealand. GNS Science
599 Report 2015/42.

600 Holden, C., Kaneko, Y., D’Anastasio, E., Benites, R., Fry, B. and I.J. Hamling (2017). The 2016
601 Kaikōura earthquake revealed by kinematic source inversion and seismic wavefield simulations:

602 Slow rupture propagation on a geometrically complex crustal fault network. *Geophysical*
603 *Research Letters*. **44**. [https://doi.org/ 10.1002/2017GL075301](https://doi.org/10.1002/2017GL075301).

604 Horspool, N., Chadwick, M., Ristau, J., Salichon, J., and M.C. Gerstenberger (2015).
605 ShakeMapNZ: Informing post-event decision making. Proceedings. Conference of the New
606 Zealand Society for Earthquake Engineering, Rotorua, April, 2015.

607 Hovius, N., Stark, C. P., and P.A. Allen (1997). Sediment flux from a mountain belt derived by
608 landslide mapping. *Geology*. **25** 231-234.

609 Hungr, O., Leroueil, S., and L. Picarelli (2014). The Varnes classification of landslide types, an
610 update. Review article. *Landslides*. **11** 167-194.

611 IRIS DMC (2013a) Data Services Products: Earthquake energy & rupture duration, doi:
612 10.17611/DP/13298836.

613 IRIS DMC (2013b) Data Services Products: Earthquake energy & rupture duration, doi:
614 10.17611/DP/1727715.

615 Jibson, R.W., Allstadt, K.E., Rengers, F.K., and J.W. Godt (2017). Overview of the geologic
616 effects of the November 14, 2016 M_w 7.8 Kaikoura, New Zealand, earthquake: U.S. Geological
617 Survey Scientific Investigations Report 2017-5146.

618 Kaiser, A.E.; Balfour, N.; Fry, B.; Holden, C.; Litchfield, N.J.; Gerstenberger, M.C.;
619 D'Anastasio, E.; Horspool, N.A.; McVerry, G.H.; Ristau, J., et al. (2017). The 2016 Kaikoura,
620 New Zealand, earthquake: Preliminary seismological report. *Seismological Research Letters*. **88**
621 1-13. doi: 10.1785/0220170018

622 Kanamori, H., and H. Heaton (2000). Microscopic and macroscopic physics of earthquakes, in
623 Geocomplexity and the Physics of Earthquakes, Geophys. Monogr. Ser., vol. 120, edited by J. B.
624 Rundle, D. L. Turcotte, and W. Klein. 147–163. doi:10.1029/GM120p0147.

625 Kaneko, Y., Fukuyama, E., and I.J. Hamling (2017). Slip-weakening distance and energy budget
626 inferred from near-fault ground deformation during the 2016 Mw 7.8 Kaikōura earthquake.
627 Geophysical Research Letters. **44** 4765-4773. doi: 10.1002/2017GL073681.

628 Keefer, D.K. (2002). Investigating landslides caused by earthquakes—A historical review.
629 Surveys in Geophysics. **23** 473–510.

630 Keefer, D.K. (2013). Landslides Generated by Earthquakes: Immediate and Long-Term Effects.
631 Treatise on Geomorphology. **5** 250-266. doi: 10.1016/B978-0-12-374739-6.00091-9250.

632 Kramer, S. L. (1996). Geotechnical earthquake engineering, Upper Saddle River, New Jersey,
633 Prentice-Hall, Inc.

634 Kutner, M. H., Neter, J., and C.J. Nachtsheim (2004). Applied Linear Regression Models, 4th
635 Edn., McGraw-Hill/Irwin, USA, ISBN-13: 978-0073014661, 2004.

636 Langridge, R.M.; Ries, W.F.; Litchfield, N.J.; Villamor, P.; Van Dissen, R.J.; Barrell, D.J.A.;
637 Rattenbury, M.S.; Heron, D.W.; Haubrock, S.; Townsend, D.B., et al. (2016). The New Zealand
638 Active Faults Database. New Zealand Journal of Geology and Geophysics. **59** 86-96.
639 doi:10.1080/00288306.2015.1112818

640 Li, G., West, J.A., Densmore, A.L., Jin, Z., Parker, R.N., and R.G. Hilton (2014). Seismic
641 mountain building: Landslides associated with the 2008 Wenchuan earthquake in the context of a

642 generalized model for earthquake volume balance. *Geochemistry, Geophysics, Geosystems*. **4**
643 833-844. doi 10.1002/2013GC005067.

644 Litchfield, N.J., P. Villamor, R.J., Van Dissen, A. Nicol, P.M. Barnes, D.J.A. Barrell, J. Pettinga,
645 R.M. Langridge, T.A. Little, J. Mountjoy, W.F., et al. (this issue). Surface fault rupture from the
646 Mw 7.8 2016 Kaikōura earthquake, New Zealand, and insights into factors controlling multi-fault
647 ruptures. *Bull. Seism. Soc. Am.*

648 Malamud, B.D., Turcotte, D.L., Guzzetti, F., and P. Reichenbach (2004). Landslide inventories
649 and their statistical properties. *Earth Surface Processes and Landforms*. **29** 687–711.

650 Marc, O., Hovius, N., Meunier, P., Gorum, T., and T. Uchida (2015). A seismologically
651 consistent expression for the total area and volume of earthquake-triggered landsliding. *Journal*
652 *of Geophysical Research: Earth Surface*. **121** 640–663. doi: 10.1002/2015JF003732.

653 Massey, C.I., Della-Pasqua, F.N., Holden, C., Kaiser, A.E., Richards, L., Wartman, J.,
654 McSaveney, M.J., Archibald, G.C., Yetton, M., and L. Janku (2016). Rock slope response to
655 strong earthquake shaking. *Landslides*. **14** 249–268. doi: 10.1007/s10346-016-0684-8.

656 Meunier, P., Hovius, N., and J. Haines (2007). Regional patterns of earthquake-triggered
657 landslides and their relation to ground motion. *Geophysical Research letters*. **34** 1-5. L20408.
658 doi:10.1029/2007GL031337.

659 Nicol, A., Khajavi, N., Pettinga, J., Fenton, C., Stahl, T., Bannister, S., Pedley, K., Hyland, N.,
660 Bushell, T., Hamling, I., et al. (this issue). Preliminary geometry, slip and kinematics of fault
661 ruptures during the 2016 Mw 7.8 Kaikōura Earthquake in the North Canterbury region of New
662 Zealand. *Bull. Seism. Soc. Am.*

663 Parker, R.N., Densmore, A.L., Rosser, N.J., de Michele, M., Li, Y., Huang, R., Whadcoat, S.,
664 and D.N. Petley (2011). Mass wasting triggered by the 2008 Wenchuan earthquake is greater
665 than orogenic growth. *Nature Geoscience*. **4** 449–452. doi:10.1038/ngeo1154.

666 Parker, R.N., Hancox, G.T., Petley, D.N., Massey, C.I., Densmore, A.L. and N.J. Rosser (2015).
667 Spatial distributions of earthquake-induced landslides and hillslope preconditioning in the
668 northwest South Island, New Zealand. *Earth Surface Dynamics*. **3** 501-525. doi: 10.5194/esurf-3-
669 501-2015.

670 Perrin, N.D., Heron, D., Kaiser A., and C. Van Houtte (2015). Vs30 and NZS 1170.5 site class
671 maps of New Zealand. (2015) New Zealand Society for Earthquake Engineering, conference.
672 New Zealand. Paper Number O-07.

673 Rai, M., Rodriguez-Marek, A., and A. Yong (2016). An empirical model to predict topographic
674 effects in strong ground motion using California small- to medium-magnitude earthquake
675 database Manisha. *Earthquake Spectra*. **32** 1033–1054.

676 Rathje, E., Little, M. Wartman, J., Athanasopoulos-Zekkos, A., Massey, C. and N. Sitar (2017).
677 Preliminary Landslide Inventory for the 2016 Kaikoura, New Zealand Earthquake Derived from
678 Satellite Imagery and Aerial/Field Reconnaissance, version 1 (January 4, 2017). Quick Report 1,
679 ver. 1 of the forthcoming NZ-US Geotechnical Extreme Events Reconnaissance (GEER)
680 Association Report on the Geotechnical Effects of the 2016 M_w 7.8 Kaikoura Earthquake.

681 Rattenbury, M.S., Townsend, D., and M.R. Johnston (compilers) (2006). *Geology of the*
682 *Kaikoura area: scale 1:250,000 geological map*. Lower Hutt: GNS Science. Institute of
683 *Geological & Nuclear Sciences 1:250,000 geological map 13*. 70 p. + 1 folded map.

684 Read, S. A. L., and P.J. Miller (1990). Characterisation and classification of New Zealand
685 Tertiary age sedimentary soft rocks. In. Bridge design and research seminar, 1990. Volume 4.
686 Road engineering in soft rock materials. RRU Bulletin **84** 1-25.

687 Scheingross, J.S., Minchew, B.M., Mackey, B.H., Simons, M., Lamb, M.P., and S. Hensley
688 (2013). Fault-zone controls on the spatial distribution of slow-moving landslides. Geological
689 Society of America. **125** 473–489.

690 Sepúlveda, S., Murphy, W., Jibson, R.W. and D.N. Petley (2005). Seismically-induced rock
691 slope failures resulting from topographic amplification of strong ground motions: The case of
692 Pacoima Canyon, California. Engineering Geology. **80** 336-348.

693 Stark, C. P. and F. Guzzetti (2009). Landslide rupture and the probability distribution of
694 mobilized debris volumes, J. Geophys. Res. Earth Surface. **114** 1–16. doi:10.1029/2008jf001008,
695 2009.

696 Stark, C.P., and N. Hovius (2001). The characterization of landslide size distributions,
697 Geophysical Research Letters. **28** 1091-1094. doi:10.1029/2000GL008527.

698 Stevenson, J.R. (2017). Economic and Social Reconnaissance: Kaikōura Earthquake 2016.
699 Bulletin of the New Zealand Society for Earthquake Engineering, Kaikoura Earthquake Special
700 Issue. **50** 343-351.

701 Stirling, M., McVerry, G., Gerstenberger, M., Litchfield, N., Van Dissen, R., Berryman, K.,
702 Barnes, P., Wallace, L., Bradley, B., Villamor, P., et al. (2012). National Seismic Hazard Model
703 for New Zealand: 2010 Update. Bull. Seism. Soc. Am. **102** 1514-1542.

704 Stirling, M.W., Litchfield, N.J., Villamore, P., Van Dissen, R. J., Nicol, A., Pettinga, J., Barnes,
705 P., Langridge, R.M., Little, T., Barrell, D. J. A., et al. (2017). The Mw 7.8 2016 Kaikoura
706 earthquake: Surface fault rupture and seismic hazard context. *Bulletin of the New Zealand*
707 *Society for Earthquake Engineering*. **50** 73-84.

708 Van Den Eeckhaut, M., Poesen, J., Govers, G., Verstraeten, G., and A. Demoulin (2007).
709 Characteristics of the size distribution of recent and historical landslides in a populated hilly
710 region. *Earth Planet. Sc. Lett.* **256** 588–603. doi:10.1016/j.epsl.2007.01.040.

711 Van Dissen, R., McSaveney, M., Townsend, D., Hancox, G., Little, T., Ries, W., Perrin, N.,
712 Archibald, G., Dellow, S., Massey, C., et al. (2013). Landslides and liquefaction generated by the
713 Cook Strait and Lake Grassmere earthquakes: A reconnaissance report. *Bulletin of the New*
714 *Zealand Society for Earthquake Engineering*. **46** 196-200.

715 Von Ruetten, J., Papritz, A., Lehmann, P., Rickli, C., and D. Or (2011). Spatial statistical
716 modelling of shallow landslides-validating predictions for different landslide inventories and
717 rainfall events. *Geomorphology*. **133** 11-22.

718 Wald, D.J., Quitoriano, V., Heaton, T. H., Kanamori, H., Scrivner C.W., and B.C., Worden
719 (1999). TriNet "ShakeMaps": Rapid generation of peak ground-motion and intensity maps for
720 earthquakes in southern California. *Earthquake Spectra*. **15** 537-556.

721 Worden, C.B., Gerstenberger, M.C., Rhoades, D.A., and D.J. Wald (2012). Probabilistic
722 relationships between ground motion parameters and Modified Mercalli Intensity in California.
723 *Bull. Seism. Soc. Am.* **102** 204-221. doi:10.1785/0120110156.

724 Xu, C., Xu, X., Yao, X., and F. Dai (2014). Three (nearly) complete inventories of landslides
725 triggered by the May 12, 2008 Wenchuan M_w 7.9 earthquake of China and their spatial
726 distribution statistical analysis. *Landslides*. **11** 441-461: doi.org/10.1007/s10346-013-0404-6.

727 Xu, C., Xu, X., Tian, Y., Shen L., Yao, Q., Huang, X., Ma, J., Chen, Xi, and S. Ma (2016). Two
728 comparable earthquakes produced greatly different coseismic landslides: the 2015 Gorkha, Nepal
729 and 2008 Wenchuan, China events. *Journal of Earth Science*. **27** 1008–1015.

730 **Full mailing address for each author**

731 C. Massey, GNS Science, PO Box 30-368, Lower Hutt 5040, New Zealand

732 D. Townsend, GNS Science, PO Box 30-368, Lower Hutt 5040, New Zealand

733 E. Rathje, University of Texas, 110 Inner Campus Drive, Austin, TX 78705, USA

734 K. Allstadt, U.S. Geological Survey, Box 25046, DFC, MS 966 Denver, CO 80225-0046, USA

735 B. Lukovic, GNS Science, PO Box 30-368, Lower Hutt 5040, New Zealand

736 Y. Kaneko, GNS Science, PO Box 30-368, Lower Hutt 5040, New Zealand

737 B. Bradley, University of Canterbury, Private Bag 4800, Christchurch 8140, New Zealand

738 J. Wartman, University of Washington, 132F More Hall, Seattle WA 98195, USA

739 R. Jibson, U.S. Geological Survey, Box 25046, DFC, MS 966 Denver, CO 80225-0046, USA

740 D.N. Petley, University of Sheffield, Western Bank, Sheffield S10 2TN, UK

741 N. Horspool, GNS Science, PO Box 30-368, Lower Hutt 5040, New Zealand

742 I. Hamling, GNS Science, PO Box 30-368, Lower Hutt 5040, New Zealand

- 743 J. Carey, GNS Science, PO Box 30-368, Lower Hutt 5040, New Zealand
- 744 S. Cox, GNS Science, PO Box 30-368, Lower Hutt 5040, New Zealand
- 745 J. Davidson, University of Canterbury, Private Bag 4800, Christchurch 8140, New Zealand
- 746 S. Dellow, GNS Science, PO Box 30-368, Lower Hutt 5040, New Zealand
- 747 J. Godt, U.S. Geological Survey, Box 25046, DFC, MS 966 Denver, CO 80225-0046, USA
- 748 C. Holden, GNS Science, PO Box 30-368, Lower Hutt 5040, New Zealand
- 749 K. Jones, GNS Science, PO Box 30-368, Lower Hutt 5040, New Zealand
- 750 A. Kaiser, GNS Science, PO Box 30-368, Lower Hutt 5040, New Zealand
- 751 M. Little, University of Texas, 110 Inner Campus Drive, Austin, TX 78705, USA
- 752 B. Lyndsell, GNS Science, PO Box 30-368, Lower Hutt 5040, New Zealand
- 753 S. McColl, Massey University, Private Bag 11 222, Palmerston North 4442, New Zealand
- 754 R. Morgenstern, GNS Science, PO Box 30-368, Lower Hutt 5040, New Zealand
- 755 F. Rengers, U.S. Geological Survey, Box 25046, DFC, MS 966 Denver, CO 80225-0046, USA
- 756 D. Rhoades, GNS Science, PO Box 30-368, Lower Hutt 5040, New Zealand
- 757 B. Rosser, GNS Science, PO Box 30-368, Lower Hutt 5040, New Zealand
- 758 D. Strong, GNS Science, PO Box 30-368, Lower Hutt 5040, New Zealand
- 759 C. Singeisen, GNS Science, PO Box 30-368, Lower Hutt 5040, New Zealand

760 M. Villeneuve, University of Canterbury, Private Bag 4800, Christchurch 8140, New Zealand

761

762 Table 1. Lithology and landslide types adopted in this paper

Lithology	Proportion of main area affected (%)	Landslide point / area density* (N/km ² / %)	Dominant landslide types
Quaternary sands, silts and gravels. These typically form river terrace deposits in the region.	19	1.8 / 0.3	Debris avalanches and flows that tend to be relatively small, and their source areas are mainly located in the terrace sands and gravels on top of the steeper coastal slopes. Many other landslides occurred within the shallow regolith, which covers many slopes in the area that were affected by strong ground shaking. These include shallow, translational slides in soil with displacements of a few centimetres to several metres.
Neogene limestones, sandstones and siltstones. These are typically massive, but weak rocks with unconfined compressive strengths (UCS) of typically <2MPa (Read and Miller, 1990).	9	5.5 / 0.9	Relatively shallow debris avalanches and flows that source from the more weathered rocks, or relatively deep-seated slides and slumps, where movement is thought to occur either along bedding or other persistent structural discontinuities, e.g., fault planes, thin clay seams, or through the rock mass. Substantial numbers of pre-Kaikoura earthquake, large landslides were mapped in these materials of which many reactivated (a few centimetres to metres) during the earthquake, forming translational and rotational slides/slumps.
Upper Cretaceous to Paleogene rocks including limestones, sandstones, siltstones and minor volcanic rocks. These are typically massive, but weak rocks with UCS of typically <2MPa.	12	4.6 / 0.5	Rockfalls and debris avalanches in areas of steeper terrain, with some slides and slumps (termed coherent after Keefer 2013) in areas of less steep topography, and their location might be controlled by the presence of thin clay seams or small-scale changes in lithology. Several relict landslides are present in these materials, and there were numerous small rockfalls and debris avalanches from their over-steep head scarps.
Lower Cretaceous Torlesse (Pahau terrane) "basement" rocks predominantly sandstones and argillite (greywacke). These are relatively strong rocks with UCS 10-20 MPa, but they are closely jointed.	60	2.5 / 0.6	Rockfalls (of individual boulders) to debris and rock avalanches. Given the highly discontinuous nature of the rock mass, most landslides are controlled by multiple intersecting joint blocks, hence a potential limitation on the volume of such failures. However, the Kaikoura earthquake triggered several very large and structurally controlled rock avalanches, the Hapuku landslide being the largest mapped landslide.

763 * Landslide point densities were calculated by dividing the number of landslide sources within a given geological
 764 unit by the area of ground within that given unit, within the main area affected by landslides (Figure 1b). Landslide
 765 area densities were calculated by dividing the total area of all landslide sources within a given geological unit by the
 766 area of ground within that unit, within the main area affected by landslides.

768 Table 2. Predictor variables evaluated in the logistic regression model, their ID codes,
 769 descriptions and units.

Variable type	Variable ID	Description	Units
Susceptibility	Geology 1	Quaternary sands, silts and gravels. These materials typically form terrace deposits on the top of the steep coastal cliffs as well as inland slopes adjacent to the main rivers of the area. Many of these terraces have been incised by rivers.	N/A
	Geology 2	Neogene limestones, sandstones and siltstones, which are typically weak. They occur along sections of the coast north of Kaikoura.	N/A
	Geology 3	Upper Cretaceous to Paleogene rocks including limestones, sandstones, siltstones and minor volcanic rocks. These are typically weak (like the Neogene limestones and sandstones), and easily erodible and they can contain thin clay seams, which are volcanic in origin. They are typically exposed in narrow strips overlying the greywacke basement rocks.	N/A
	Geology 4	Lower Cretaceous Torlesse (Pahau terrane) “basement” rocks are predominantly sandstones and argillite, also known as greywacke. The greywacke rocks are typically moderately to well bedded and tend to be closely jointed. They form many of the coastal slopes as well as the steeper inland Kaikoura mountain ranges.	N/A
	Slope _{MEAN}	Local hillslope gradient taken from the 8 m resolution digital elevation model generated by GNS Science, adopting the mean value of all of the 8 m by 8 m cells that fall within each cell of the sample 32 m by 32 m grid. This variable is a proxy for the static shear stresses in the slope.	Deg (°)
	Elev _{MEAN}	Local hillslope elevation taken from the 8 m resolution digital elevation model generated by GNS Science, adopting the mean value of all of the 8 m by 8 m cells that fall within the each cell of the sample 32 m by 32 m grid. This variable represents the observation that topography can limit the size of the landslides. For example, slopes that are higher in elevation tend to have larger surface areas, and can therefore generate larger landslides than slopes at lower elevations, which tend to have smaller surface areas.	mAMSL
	Curv _{PROFILE}	Profile curvature generated using ArcGIS, taken from the curvature of the surface on a cell-by-cell basis, as fitted through that cell and its eight surrounding	One hundredth

		neighbours. using the 8 m resolution digital elevation model generated by GNS Science. A negative value indicates the surface is upwardly convex at that cell. A positive profile indicates the surface is upwardly concave at that cell. A value of 0 indicates the surface is flat. This variable is a proxy for slope “sharpness” that represents topographic amplification effects, as amplification of shaking has been recorded at sharp breaks in slope (e.g., Massey et al., 2016; Janku, 2017).	(1/100) of a z-unit
	ASP _{MEAN}	The aspect for each sample grid-cell was calculated using ArcGIS using the 8 m resolution digital elevation model generated by GNS Science, adopting the mean of all of the 8 m by 8 m cells that fall within each cell of the 32 m by 32 m sample grid.	Deg (°)
Earthquake forcing	FaultDist	The distance from the centroid of each of the 32 m by 32 m sample grid cells to the nearest fault that ruptured using the mapped surface expression, taken from the GNS Science Active Faults database (Langridge et al., 2016), which includes those faults that ruptured during the Kaikoura earthquake.	Meters
	PGA _{SM}	Grid of the mean peak ground acceleration (PGA) derived from ShakeMap NZ (GeoNet, 2016), developed by the U.S. Geological Survey (Wald, 1999; Worden, 2012), and calibrated for New Zealand by Horspool et al. (2015). Grid resolution is 1000 m by 1000 m. The PGA values were attributed to the sample grid cell, by taking the PGV value at its centroid.	g
	PGV _{SM}	Grid of the mean peak ground velocity (PGV) derived from ShakeMap NZ. Grid resolution is 1000 m by 1000 m. The PGV values were attributed to the sample grid cell, by taking the PGV value at its centroid.	m/s
	PGV _{LF}	Low-frequency (long period) PGV calculated from waveforms up to 0.33 Hz, using the method described by Holden et al. (2017). Grid resolution is 500 m by 500 m. The PGV values were attributed to the sample grid cell, by taking the PGV value at its centroid.	m/s
	PGV _{BRADLEY}	Grid of PGV derived from modelling carried out by Bradley et al. (2017). Grid resolution is 990 m by 990 m. The PGV values were attributed to the sample grid cell, by taking the PGV value at its centroid.	m/s
	PGV _{MEAN}	Mean PGV calculated for each of the sample grid cells by sampling the PGV value from each of the three PGV models model at the centroid of each sample grid, and taking the mean of the three values.	m/s

	Disp _v	The vertical permanent tectonic displacement caused by the earthquake was taken from the 100 m by 100 m resolution three-dimensional displacement field derived from satellite radar and GPS data (Hamling et al., 2017). This variable is a proxy for ground shaking intensity because areas of increasing permanent tectonic displacement should correlate with increased dynamic ground shaking and inertial loading on the soil and rock masses forming the slopes, leading to an increase in landsliding.	Meters
	Disp _H	The horizontal permanent tectonic displacement was calculated for each sample grid cell as the vector of the maximum x and y displacement fields taken from Hamling et al. (2017), 100 m by 100 m resolution three-dimensional displacement field. As Disp _v , this variable is a proxy for ground-shaking intensity.	Meters
	LSR	Local slope relief calculated using focal statistics in ArcGIS. It represents the local height (and angle) of the sample grid cell. It is calculated as the difference in elevation between the lowest in elevation 8 m by 8 m grid cell, within an 80 m (ten (10) 8 m cells) radius from the centroid of the given sample grid cell, and the mean elevation of that grid cell (Elev _{MEAN}). This variable represents a proxy for slopes that could amplify ground shaking due to their “larger-scale steepness” (larger than just a sample grid-cell size), where larger values of LSR represent the steeper and higher slopes of the region, which can amplify ground shaking more than lower in height and less steep slopes (Ashford et al. 1997; Massey et al., 2016).	Meters (m)

771 Table 3. Logistic regression output coefficients and model fit statistics. Input ground-motion
 772 variable PGA_{SM} . Binomial logistic regression – modelled probability that Landslide = 1.

Variable	Coefficient (c)	Standard error	95% confidence interval	
			Lower bound	Upper bound
Intercept	-8.2531	0.0471	-8.3454	-8.1608
PGA_{SM}	0.0278	0.0005	0.0268	0.0288
FaultDist	-0.0002	0.000003	-0.0002	-0.0002
$Elev_{MEAN}$	-0.0014	0.00002	-0.0014	-0.0013
$Slope_{MEAN}$	0.0816	0.0012	0.0793	0.0840
LSR	0.0158	0.0006	0.0146	0.0169
Geology 1	0.5813	0.0196	0.5429	0.6197
Geology 2	0.1963	0.0186	0.1599	0.2327
Geology 3	-0.1466	0.0104	-0.3117	-0.2434
Geology 4	-0.6866	0.0084	-0.7031	-0.6700

773
 774 Number of observations: 3,481,858. Likelihood ratio X^2 : 3.41×10^4 . All variables have p values of less than
 775 1×10^{-8} . Pseudo R^2 : 0.141

776 Table 4. Logistic regression output coefficients and model fit statistics. input ground-motion
 777 variable PGV_{SM} . Binomial logistic regression – modelled probability that Landslide = 1.

Variable	Coefficient (c)	Standard error	95% confidence interval	
			Lower bound	Upper bound
Intercept	-8.5968	0.0494	-8.6937	-8.4999
PGV_{MEAN}	0.0294	0.0005	0.0284	0.0303
FaultDist	-0.0002	0.000003	-0.0002	-0.0002
$Elev_{MEAN}$	-0.0013	0.00002	-0.0013	-0.0012
$Slope_{MEAN}$	0.0835	0.0012	0.0812	0.0858
LSR	0.0158	0.0006	0.0147	0.0170
Geology 1	0.1537	0.0214	0.1117	0.1957
Geology 2	0.3005	0.0188	0.2637	0.3372
Geology 3	-0.0978	0.0174	-0.1320	-0.0636
Geology 4	-0.3563	0.0137	-0.3831	-0.3295

778 Number of observations: 3,481,858. Likelihood ratio X^2 : 3.49×10^4 . All variables have p values of less than
 779 1×10^{-8} . Pseudo R^2 : 0.144

780

781 **List of Figure Captions**

782 Figure 1. Inset map shows the area of New Zealand affected by coseismic landslides
783 triggered by the M_w 7.8 2016 Kaikoura earthquake. a) Shows the mapped 10195 coseismic
784 landslide source areas and their size (area) triggered by the earthquake, superimposed on the 8 m
785 by 8 m digital elevation model for New Zealand, classified by elevation in meters above sea
786 level. b) The landslide source area distribution overlain on the main geological units. c)
787 Landslide source area distribution shown on the 8 m ground resolution digital elevation model
788 for New Zealand.

789 Figure 2. a) The number of landslides (frequency) with source areas within each source area
790 bin. Landslide source-area bin widths are equal in logarithmic space for all data sets. b)
791 Landslide probability density plotted against landslide area (for the landslide source areas only),
792 for landslides generated by the Kaikoura earthquake, the M_w 7.1 1968 Inangahua, New Zealand
793 earthquake (Hancox et al., 2014) and the M_w 7.8 1929 Murchison, New Zealand earthquake
794 (Hancox et al., 2016). For Figure 2b the power-law fitting statistics are: 1) M_w 7.8 2016
795 Kaikoura earthquake, where $N_{LT} = 10195$, $x_{min} = 500 \text{ m}^2$ and $\alpha = 1.88$; 2) M_w 7.8 1929
796 Murchison earthquake (Hancox et al., 2016), where $N_{LT} = 6104$, $x_{min} = 10000 \text{ m}^2$ and $\alpha = 2.62$;
797 and 3) the M_w 7.1 1968 Inangahua earthquake (Hancox et al., 2014), where $N_{LT} = 1199$, $x_{min} =$
798 10000 m^2 and $\alpha = 2.71$.

799 Figure 3. a) Hapuku rock avalanche in Lower Cretaceous basement rocks – this is the
800 largest of the mapped landslides with an estimated volume of about $20 (\pm 2) \text{ M m}^3$. In this case,
801 the slide surface appears to correspond to multiple persistent discontinuities such as old and
802 recent fault planes. Several faults that ruptured to the surface pass through the source area of the
803 landslide. The debris left the source and blocked the Hapuku River creating a dam about 100 m

804 high. Multiple lobes of debris of different clast size can be mapped in the deposit, indicating
805 multiple pulses of debris deposition. The dam subsequently overtopped and the downstream face
806 was partially eroded (due to headward erosion initiated by seepage through the dam) following
807 Cyclone Cook in April 2017. The debris left in the source is still unstable and several debris
808 flows have occurred, which have eroded the debris down to bedrock in places. The debris
809 forming the dam continues to erode as water from the impounded lake flows over the crest and
810 down the outflow channel. b) Seafront rock slide/slump in Paleogene limestone – This is the
811 largest mapped landslide in these materials with an approximate volume of $18 (\pm 2) \text{ M m}^3$. This
812 slide surface is assumed to be deep seated ($>100 \text{ m}$ below the surface), with the field
813 observations and cross sections suggesting a semi-rotational failure through the rock mass. Much
814 of the debris has remained intact, and so the slide/slump would be classified as coherent (Keefer,
815 2013). The displaced mass is still creeping and several debris flows have occurred off the toe of
816 the intact displaced debris and also the head scarp. The Papatea fault (Hamling et al., 2017)
817 ruptured through the source area suggesting that surface rupture of this fault caused the landslide
818 to initiate. The vertical displacement of this fault measured approximately 0.5 km away from the
819 landslide is about 6 m . We are not sure whether the landslide initiated either from permanent
820 coseismic displacement of the ground or dynamic displacement caused by shaking, or some
821 combination of both. c) Leader River rock slide/slump in Neogene mudstone – The largest
822 mapped landslide in these materials is the Leader River landslide with an approximate volume of
823 $8 (\pm 1) \text{ M m}^3$. This rock slide/slump is predominantly within Neogene mudstone (including
824 sandstone and siltstone), and the slide surface is assumed to be deep seated (about 80 m below
825 the surface) with the displacement vectors suggesting a translational failure (with some rotation
826 at the head scarp), possibly along bedding, which is inclined at about 20° to 25° out of the slope

827 (measured near the toe of the debris) and has the same dip direction as the vectors of landslide
828 displacement. A faulted contact between the Lower Cretaceous greywacke and Neogene
829 mudstone is also present in the landslide head scarp. Although there is no field-evidence to
830 suggest this contact ruptured, it is possible that a fault also ruptured through the source area of
831 this landslide (Nicol et al., this issue), but more investigation is needed to determine whether this
832 is the case or not. All photos D. Townsend.

833 Figure 4. Peak ground velocities (PGV) and peak ground accelerations (PGA) from: a) Bradley
834 et al. (2017) ($PGV_{BRADLEY}$), calculated up to frequencies of >10 Hz, grid resolution 1000 m; b)
835 PGV_{LF} calculated using the method by Holden et al. (2017) up to a frequency of 0.33Hz, grid
836 resolution 500 m; and c) PGV_{SM} from Shake Map NZ (median estimates), calculated up to
837 frequencies of 50 Hz, grid resolution 1000 m. d) PGA_{SM} from Shake Map NZ (median
838 estimates), calculated up to frequencies of 50 Hz, grid resolution 1000 m. The Kaikoura
839 earthquake landslide distribution (shown as grey polygons, $N=10195$ landslides) are overlain on
840 all the maps.

841 Figure 5. Permanent ground displacement: a) horizontal; and b) Vertical, and the inferred fault
842 model taken from InSAR and GPS measurements relating to the Kaikoura earthquake presented
843 by Hamling et al. (2017), grid resolution of 100 m by 100 m, overlain by the Kaikoura
844 earthquake landslide distribution (shown as grey polygons, $N=10195$ landslides).

845 Figure 6. Maps a) to d) showing the distributions of the main susceptibility predictor variables
846 used in the logistic regression model. a) Elevation ($Elev_{MEAN}$); b) Slope ($Slope_{MEAN}$); c) Distance
847 to fault ($FaultDist$); d) Local slope relief (LSR). Maps e) and f) show the estimated landslide
848 probabilities (P_{LS}) from the logistic regression model: e) adopting the PGA_{SM} variable as the

849 input ground motion; f) adopting the PGV_{SM} variable as the input ground motion. The faults that
850 ruptured to the surface during the earthquake are shown as red lines.

851 Figure 7. Consistency of the logistic regression model probabilities with the data, adopting the
852 variables listed in Table 3 and ground motion parameter PGV_{SM} . The graph shows a comparison
853 of observed and predicted landslide probabilities, calculated by accumulating (adding) the
854 predicted landslide probability (P_{LS}) values for each sample grid cell from smallest to largest,
855 along with the corresponding observed Y value for the same grid cell.

856 Figure 8. Logistic regression model performance adopting the variables listed in Table 4 and
857 ground motion parameter PGV_{SM} . The graph shows the relative contributions of predictor
858 variable to the fit of the overall model. The sequence of model variables and the resulting pseudo
859 R^2 values are shown in rank order of their significance, which we determined by sequentially
860 removing each of the predictor variables contributing least to the fit of the model.

861 Figure 9. Landslide point and area density ($N=10195$ landslides) within each 200 m distance
862 from fault buffer. Landslide density is calculated by taking the centroid of each landslide source
863 area that falls within each 200 m distance buffer from the mapped surface expression of the
864 faults that ruptured during the earthquake. The number (N) of landslide points within each
865 distance from fault bin range is then divided by the area of slope (km^2) within each bin. The
866 landslide area density is also shown, which is calculated in the same way as the landslide point
867 density; however, the area of each landslide source (km^2) within each distance from fault bin is
868 summed and divided by the total area of ground within each 200 m bin.

869 Figure 10. Landslide source areas ($N=10195$ landslides) normalised relative to the largest
870 mapped landslide (area in km^2) and their associated elevation and slope angle taken from the 8 m

871 by 8 m New Zealand digital elevation model. The slope angle and elevation values attributed to
872 each landslide source area were sampled from the digital elevation grid by calculating the mean
873 values within each source area polygon. a) Landslides on coastal slopes only; and b) landslides
874 on non-coastal slopes. c) Area of slope within a given slope angle bin as a proportion of the total
875 area of coastal and non-coastal slopes. d) Landslide point density for each slope angle bin
876 adopting 10-degree bins. Landslide density is calculated by taking the number of landslide
877 sources that have mean slope angles that are within each 10-degree slope-angle bin range. The
878 number (N) of landslides within each slope-angle bin range is then divided by the area of slope
879 (km^2) within each bin. The point densities are calculated for coastal and non-coastal slopes and
880 landslides.

881

882

883 **Appendices**

884 The information contained in the appendices comprise the following: 1) A summary of the imagery and topographic data used to map Version
 885 1.0 of the landslide distribution presented in the paper; and 2) The variance inflation factor matrix (VIF), which was used as a method to ensure
 886 that the predictor variables included in the logistic regression model did not exhibit multicollinearity.

887 Table A1. Summary of data used to compile the landslide inventory.

	Item	Data	Type	Date (NZST)	Source	Ground resolution (m)	Public availability	Notes
Pre Kaikoura earthquake data	1	Kaikoura District aerial photographs	Orthorectified mosaics Individual tiled tiffs (provided by Council) converted to one mosaic by GNS Science.	2014-2015	Environment Canterbury (ECAN), (captured by Aerial Surveys)	0.3	Yes	
	2	Marlborough District aerial photographs	Orthorectified mosaic Individual tiled tiffs (provided by Council) converted to one mosaic by GNS Science.	2011-2012	Marlborough District Council (MDC), (captured by Aerial Surveys)	0.4	Yes	
		Marlborough District aerial photographs	Orthorectified mosaic Individual tiled tiff format files	2015-2016	MDC, captured by AAM Group Ltd.	0.2	Early 2018	
	3	Kaikoura Digital Surface Model (DSM), generated from the photographs taken for 1 and 2.	ESRI Grid file	2014-2015	ECAN, captured by Aerial Surveys Ltd.	1.0	Early 2018	
	4		ESRI Grid file already provided	2014-2015	ECAN, captured by Aerial Surveys Ltd.	10.0	Early 2018	

	5	Airborne lidar	Point clouds converted to Digital Elevation Models (DEMs) and Hillshades by GNS Science	2012	Captured by AAM Group Ltd.	1.0	Yes	Only the coastal strip from Ward through to Cheviot
Post Kaikoura earthquake data	5	WorldView-2 satellite imagery	Multispectral bands supplied raw. Orthorectified as an Imagine file and converted to mosaics by GNS Science	22 November 2016	Captured by Digital Globe	2.4	Yes	EAGLE technology processed the same raw images and provided to all of government.
	6	WorldView-3 satellite imagery		15 November 2016	Captured by Digital Globe	1.4	Yes	
	7	GeoEye satellite imagery		15 November 2016	Captured by Digital Globe	2.0	Yes	
	8	Aerial photographs	RGB stereo-tiff files with image coordinates, processed to individual orthorectified images and DSMs by GNS Science. Aerial Surveys to provide complete processed data set	December 2016	Captured by Aerial surveys Ltd. commissioned by LINZ at the request of GNS Science and other New Zealand agencies	0.3	Early 2018	Area covered is the main area affected by landslides and the total area affected by landslides.
	9	Airborne LIDAR	Point clouds converted to DEM and Hillshades by GNS	November to December 2016	Captured by AAM Group Ltd. commissioned by LINZ at the request of GNS Science and other New Zealand agencies	1.0	On request	Only the coastal strip, main faults and Goose Bay provided to date. Additional areas (dam sites) to be provided later.
	10	Terrestrial LIDAR of landslides and landslide dams on the rivers called – Hapuku, Ote	Point clouds, orthorectified images,	November and December 2016	Captured by GNS Science	Variable	Yes	Multiple surveys of each dam. Several of the dams failed following Cyclone Debbie and Cook, and

		Makura, Linton, Conway, Towy, Stanton and Leader		March, April, May and September 2017					surveys of these dams were carried out post failure.
--	--	--	--	---	--	--	--	--	---

888

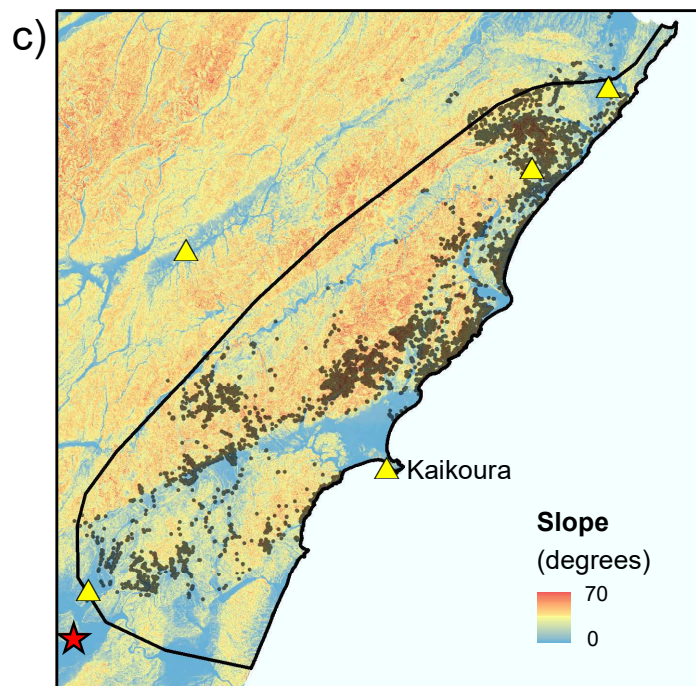
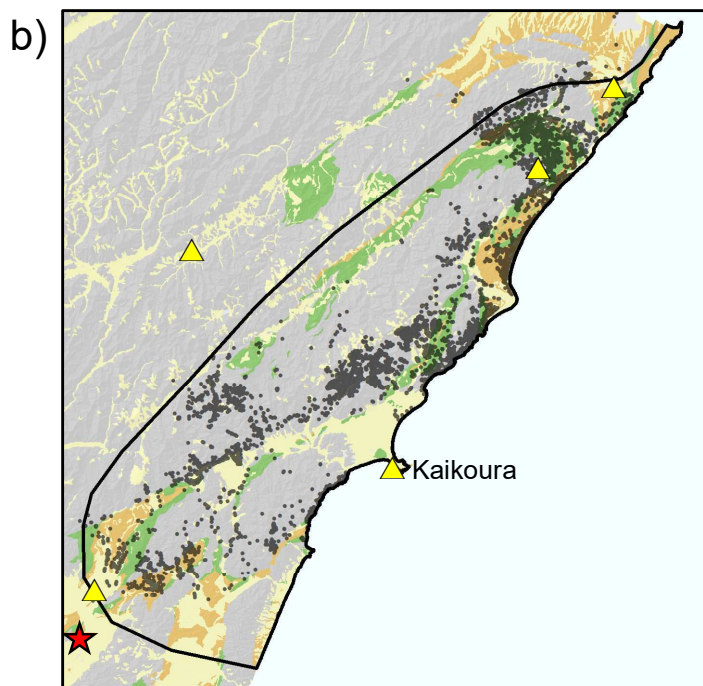
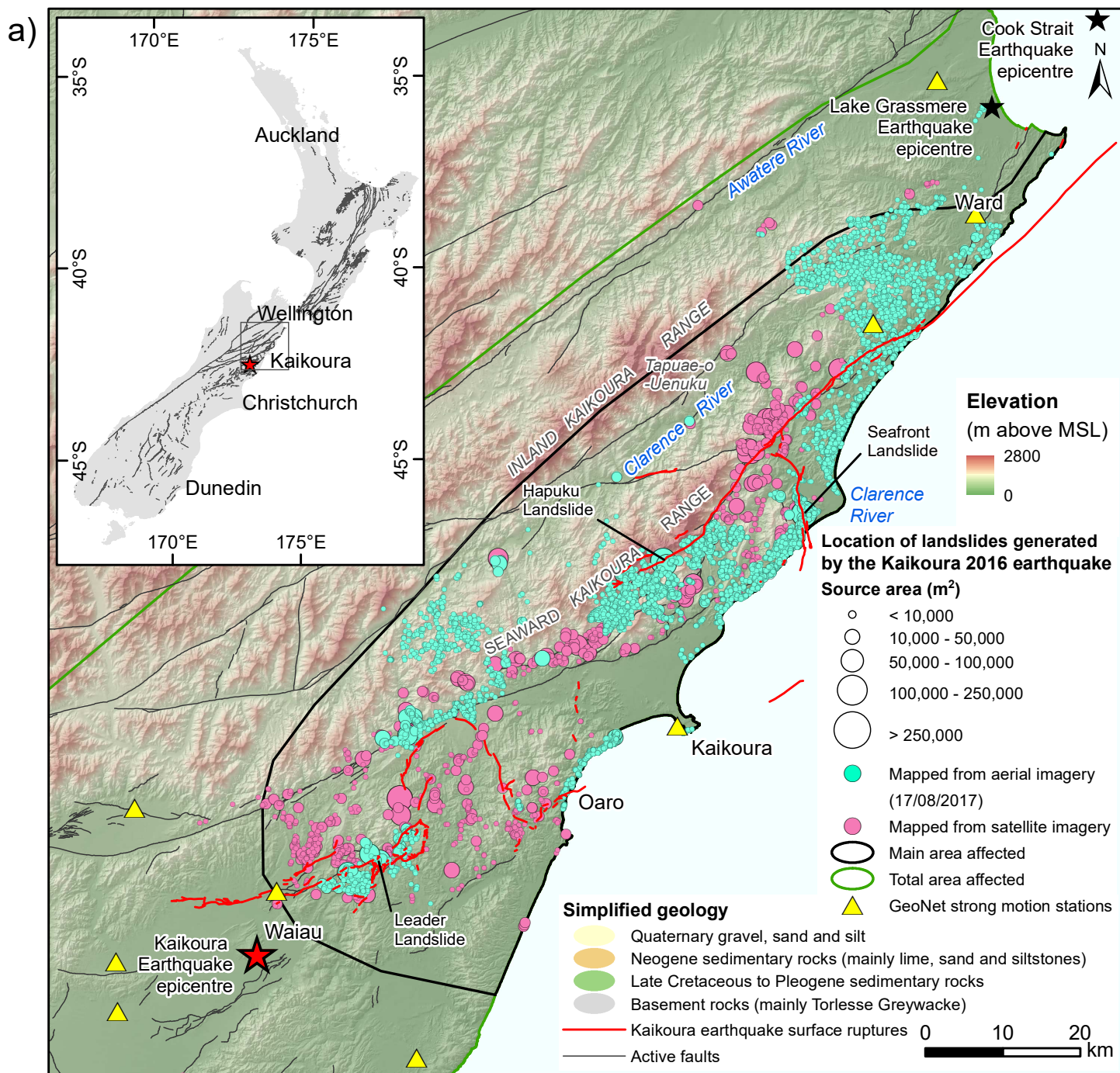
889

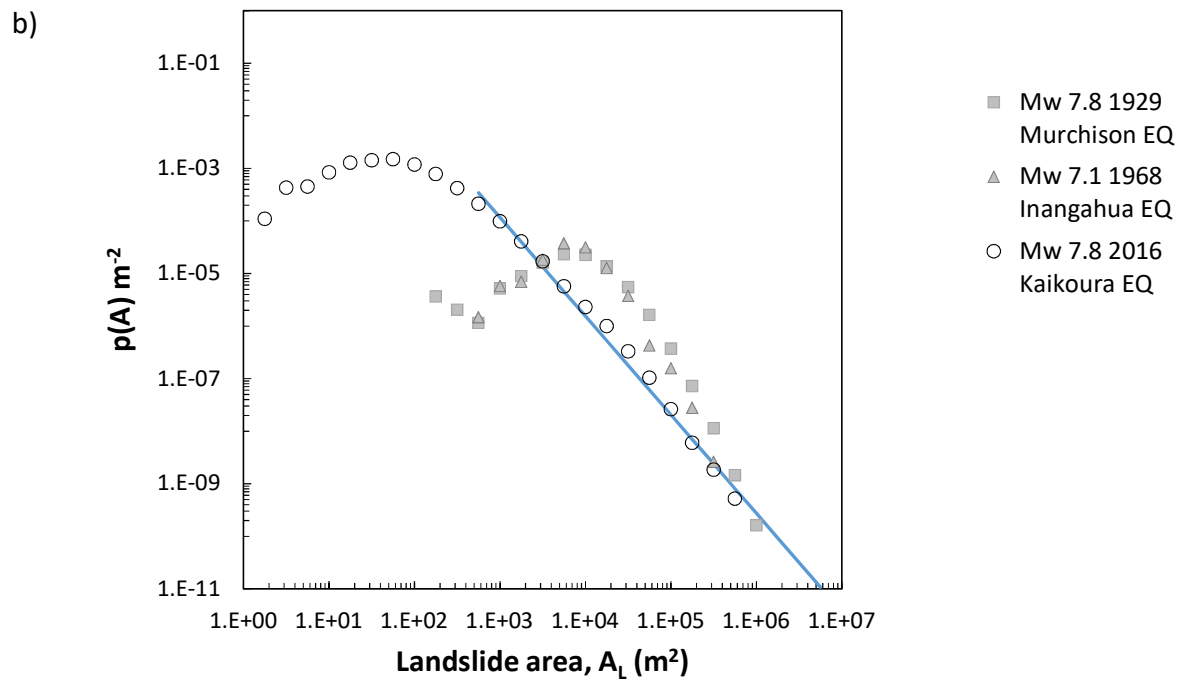
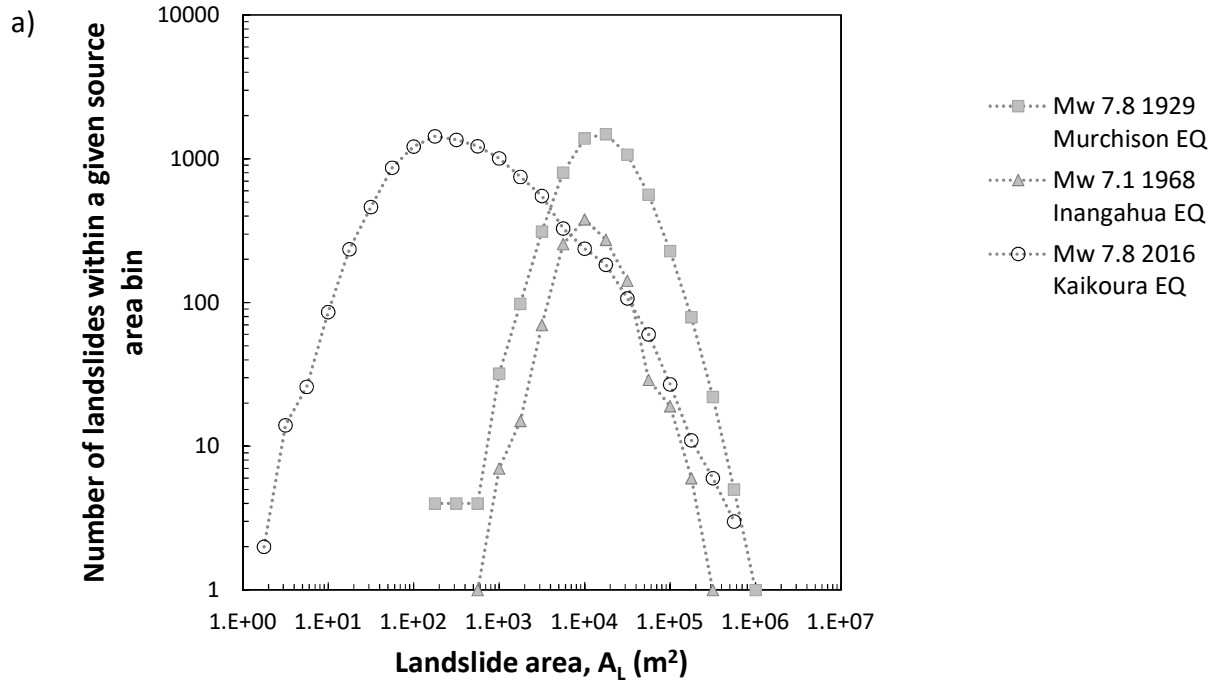
890 Table A2. Variance inflation factor matrix (VIF) for the variables included in the logistic regression models. VIF values greater than 10 indicate
 891 a high level of multicollinearity (Kutner et al., 2004) and are avoided in our models.

Variables	LSR	Slope _{MEAN}	Elev _{MEAN}	FaultDist	PGV _{MEAN}	PGV _{BRADLEY}	PGV _{LF}	PGV _{SM}	PGA _{SM}
LSR	-	4.54	1.60	1.00	1.01	1.03	1.03	1.13	1.00
Slope _{MEAN}		-	1.48	1.00	1.00	1.03	1.03	1.16	1.00
Elev _{MEAN}			-	1.04	1.00	1.00	1.02	1.11	1.02
FaultDist				-	1.10	1.04	1.02	1.30	1.60
PGV _{MEAN}					-	8.89	3.04	1.09	1.16
PGV _{BRADLEY}						-	1.96	1.00	1.05
PGV _{LF}							-	1.00	1.03
PGV _{SM}								-	1.62
PGA _{SM}									-

892

Figure 1





a)

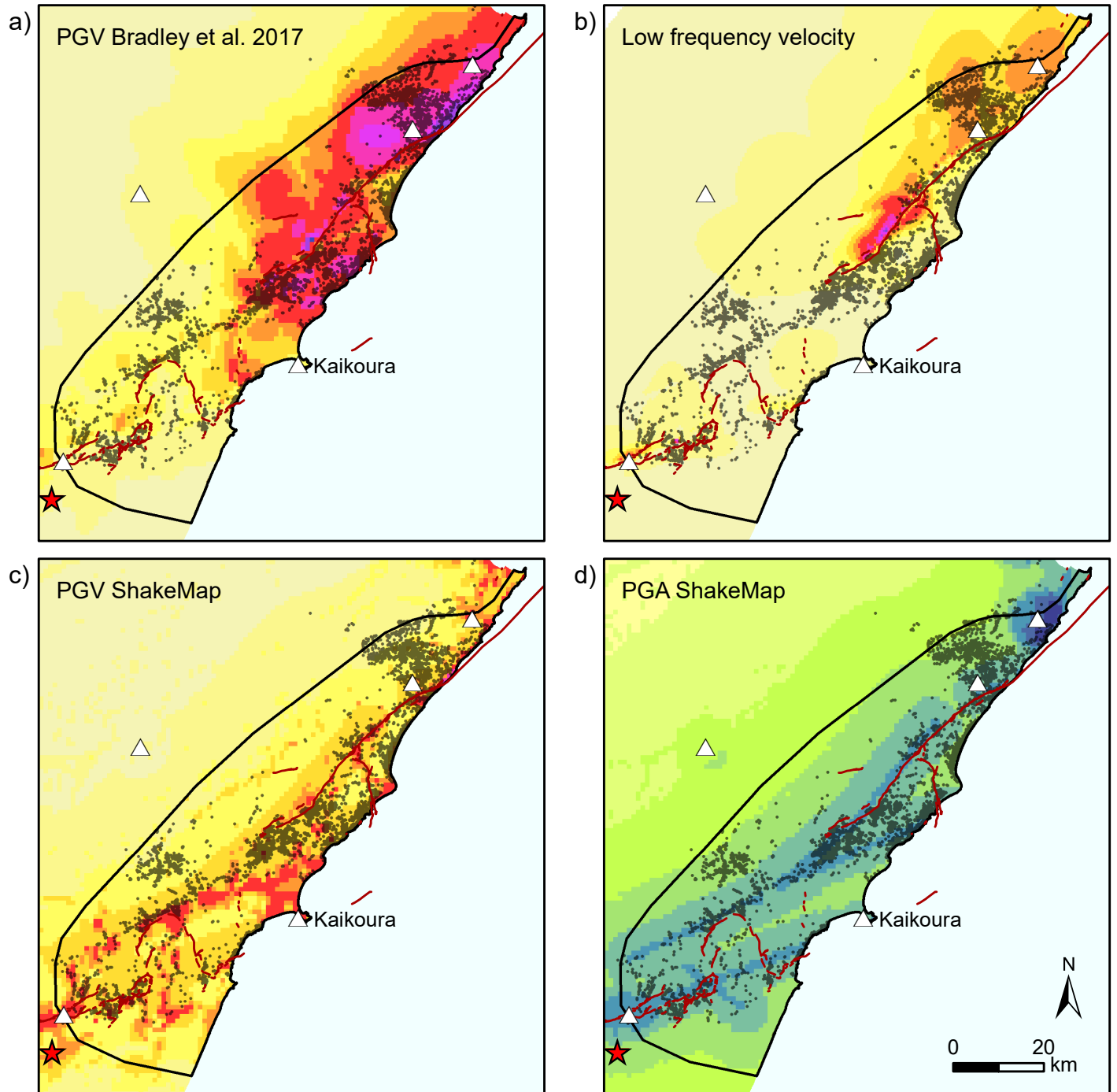


b)



c)





★ Earthquake epicentre

— Kaikoura earthquake surface ruptures

· Mapped landslides (20/08/2017)

△ GeoNet strong motion stations

PGV (cm/s)

< 20

20 - 40

40 - 60

60 - 80

80 - 100

100 - 150

150 - 200

200 - 250

250 - 300

300 - 350

> 350

PGA (g)

< 0.1

0.1 - 0.2

0.2 - 0.4

0.4 - 0.6

0.6 - 0.8

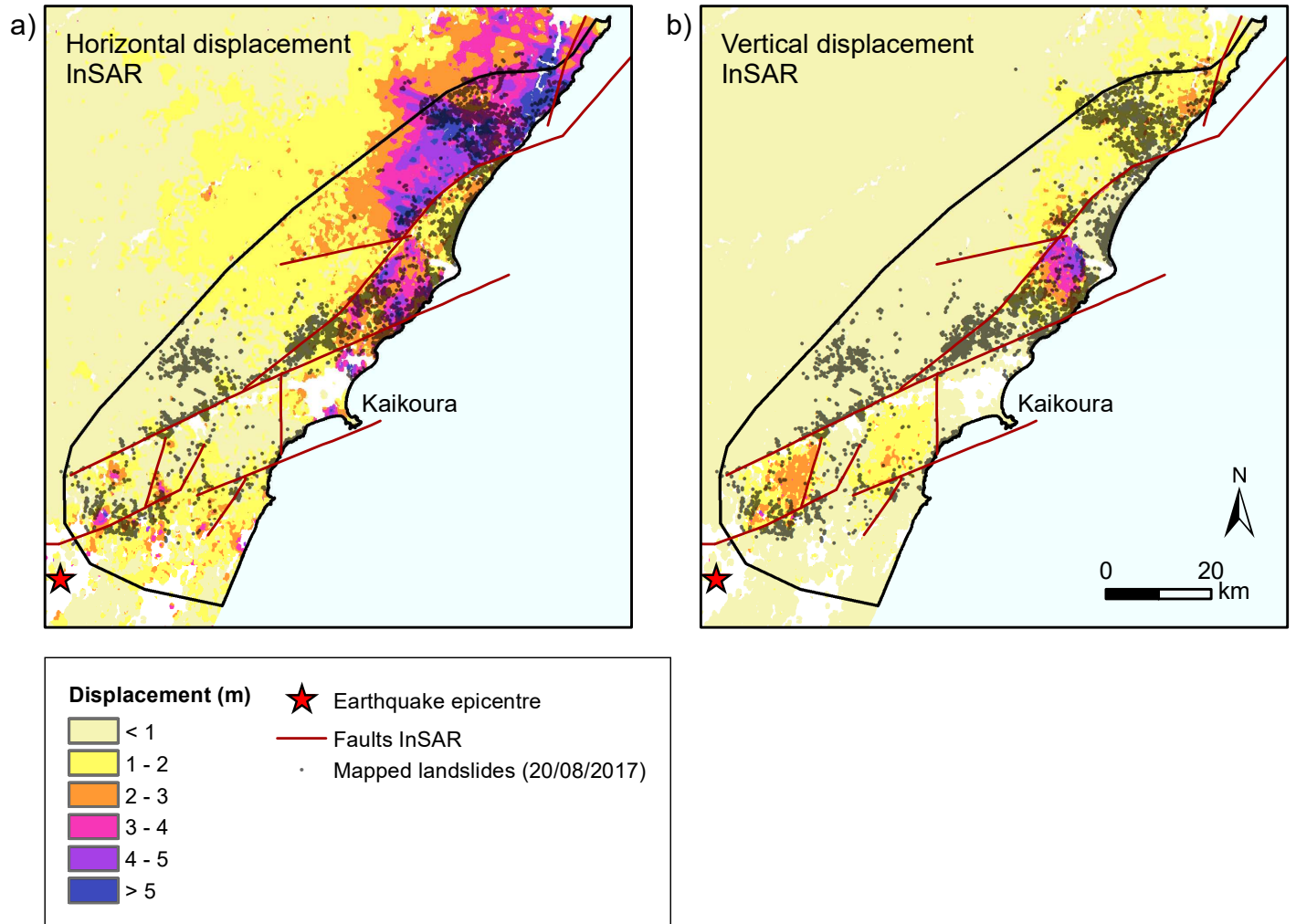
0.8 - 1.0

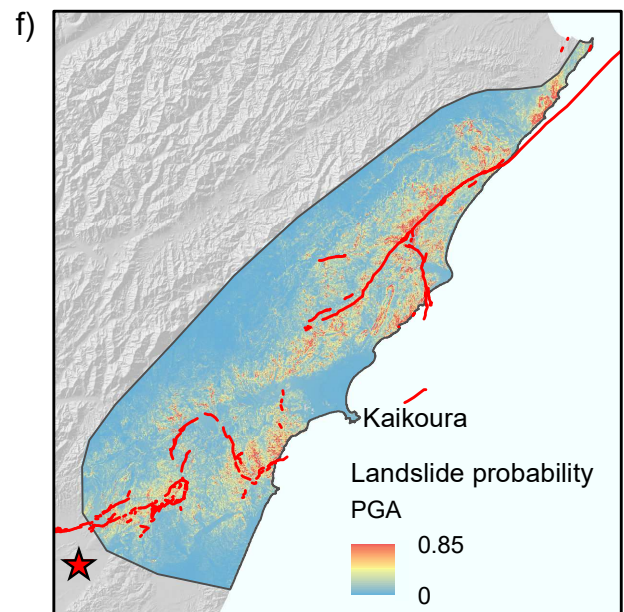
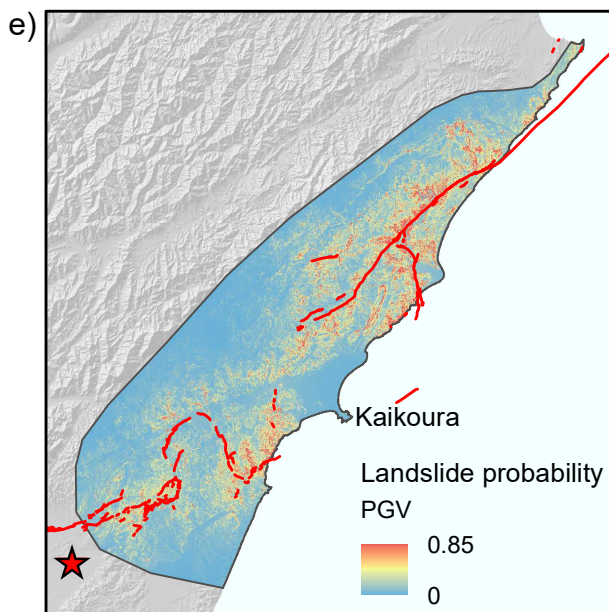
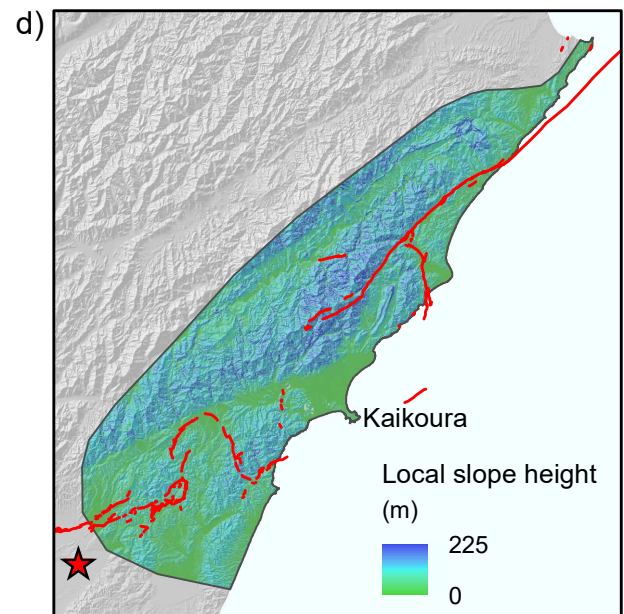
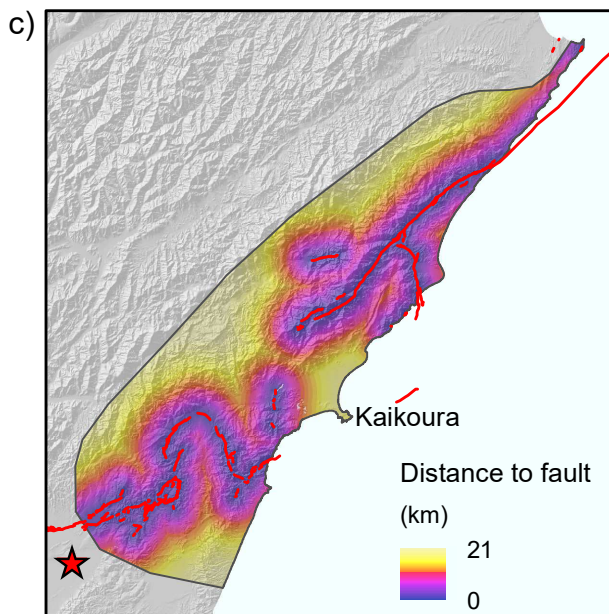
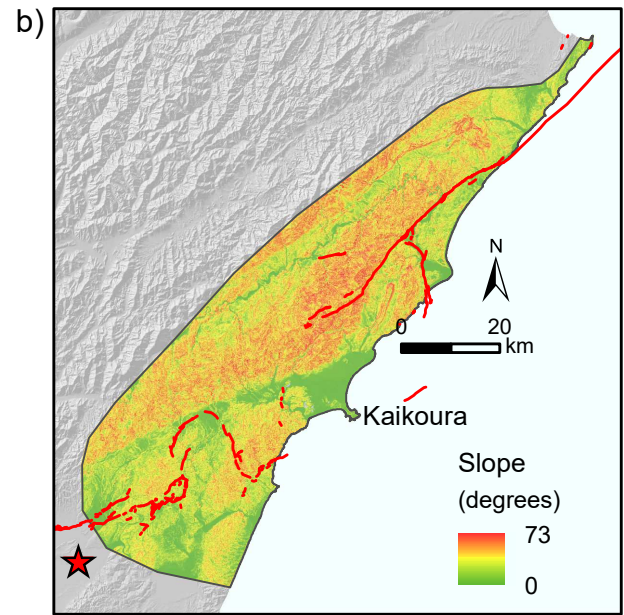
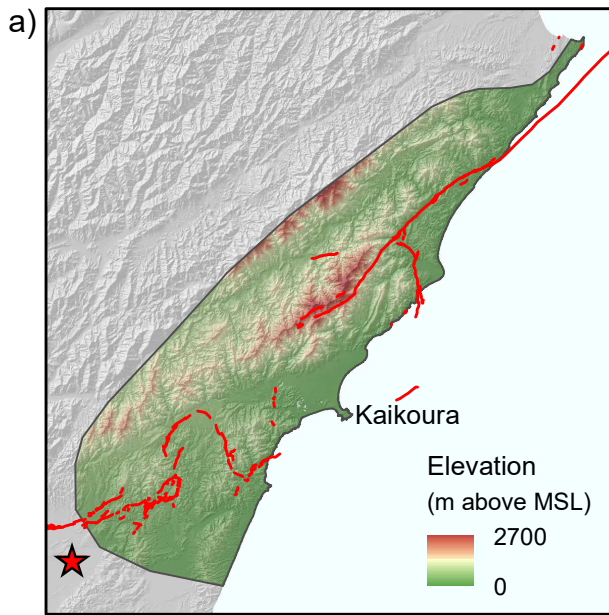
1.0 - 1.2

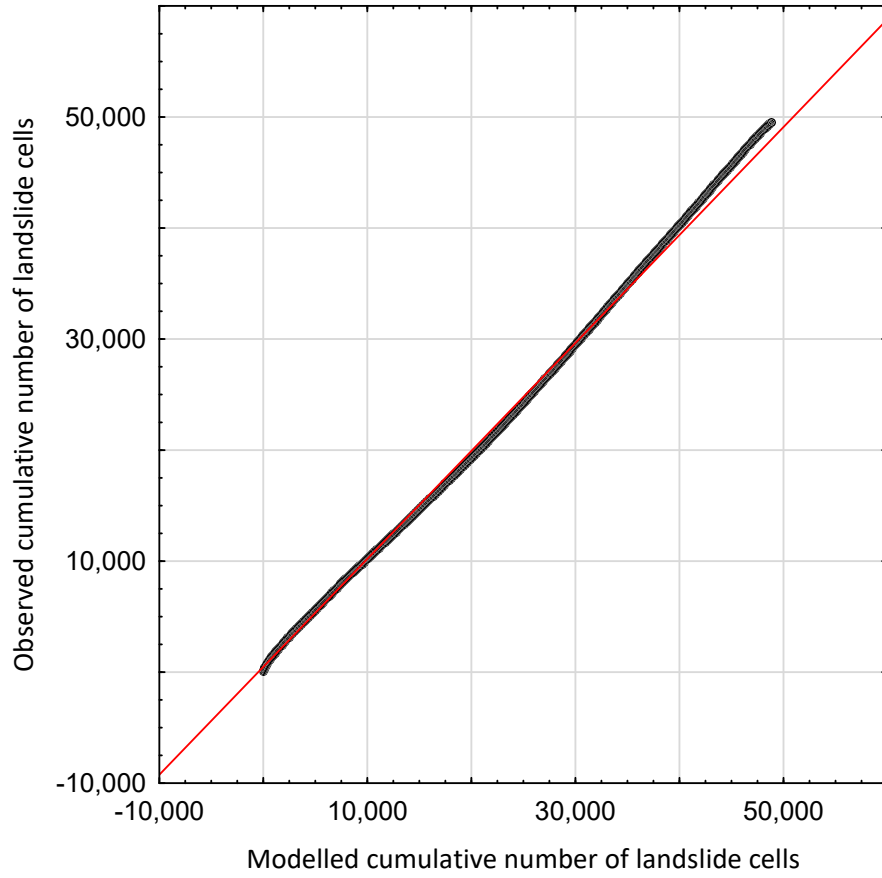
1.2 - 1.4

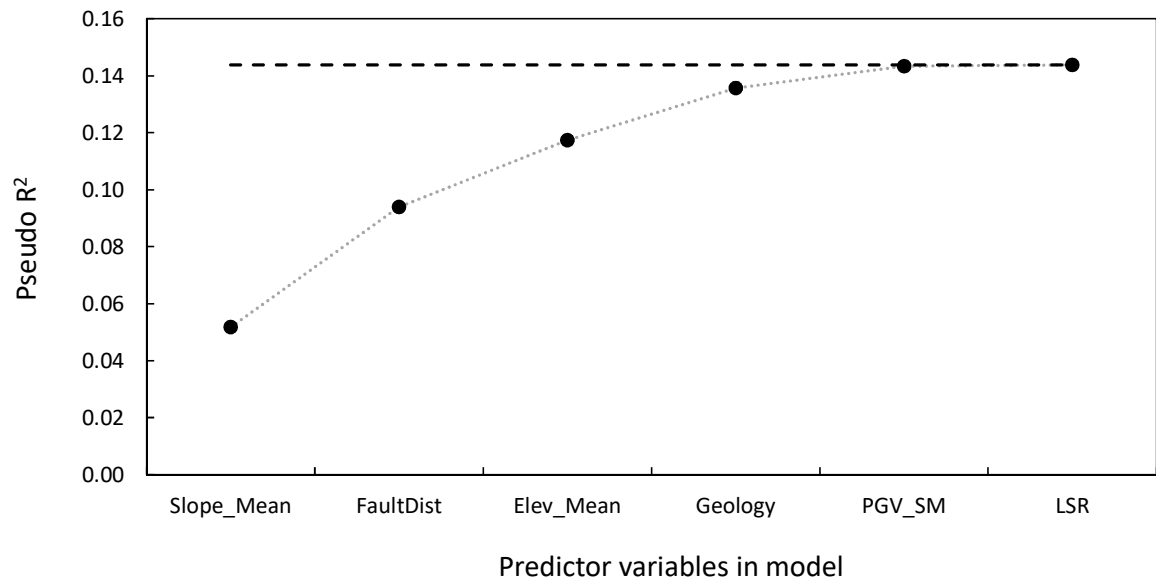
0 20 km

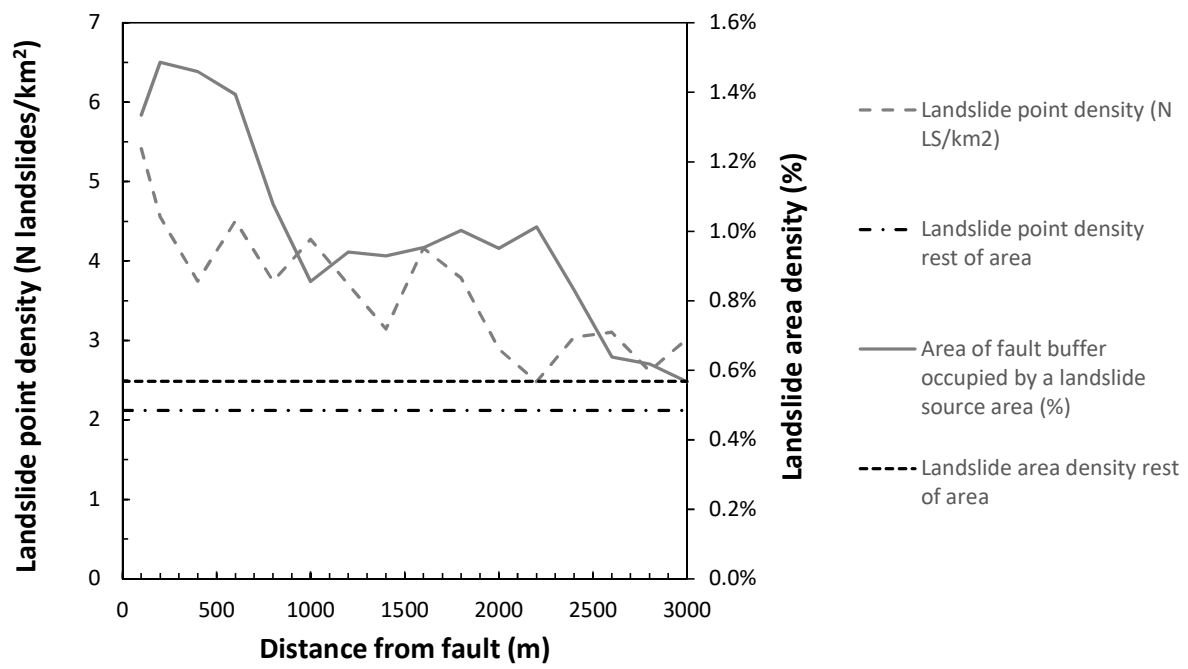
N

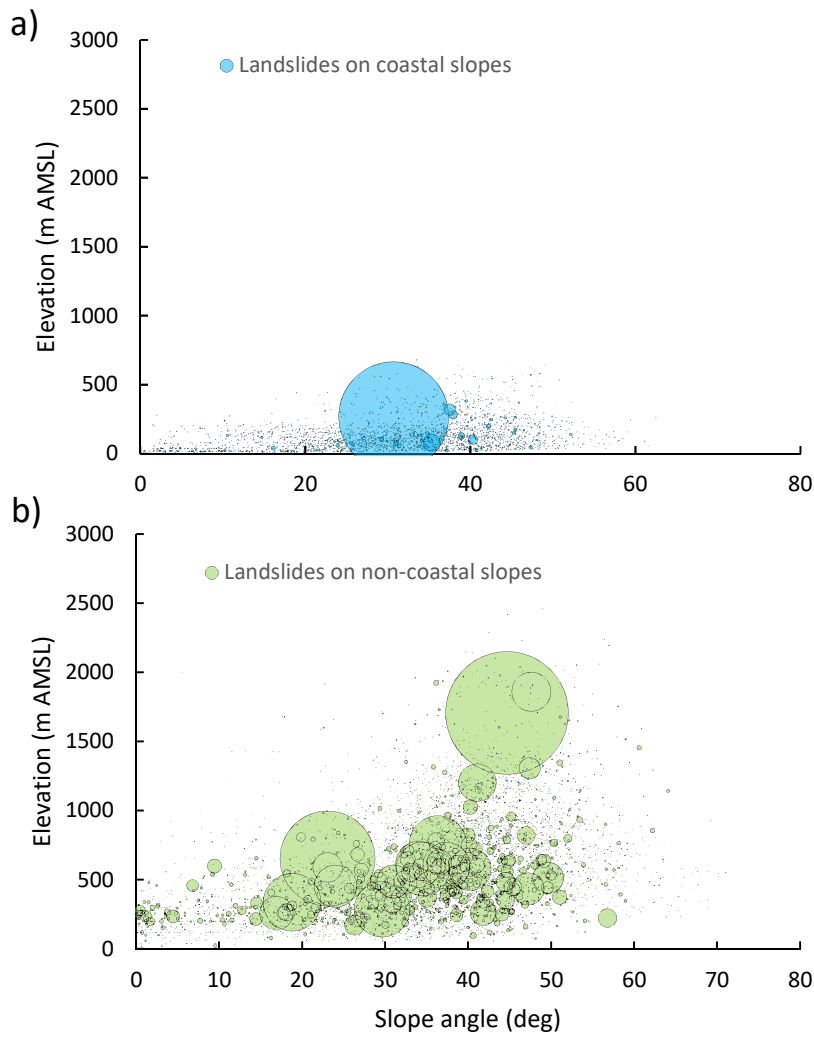


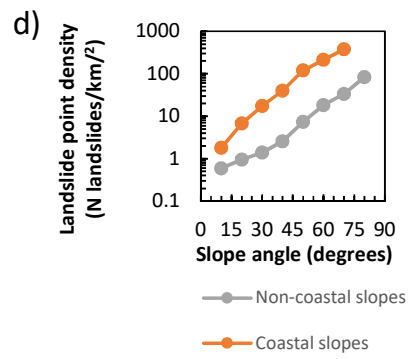
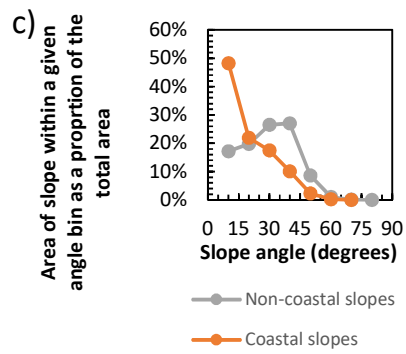












Bulletin of the Seismological Society of America

COPYRIGHT/PUBLICATION-CHARGES FORM

PLEASE FILL OUT AND SUBMIT THIS FORM ONLINE WHEN SUBMITTING YOUR PAPER

Manuscript Number: BSSA-D- _____ [leave blank for new submissions]

Title: Landslides triggered by the MW 7.8 14 November 2016 Kaikoura Earthquake, New Zealand

Authors: Chris Massey _____

COPYRIGHT

In accordance with Public Law 94-533, copyright to the article listed above is hereby transferred to the Seismological Society of America (for U.S. Government employees, to the extent transferable) effective if and when the article is accepted for publication in the *Bulletin of the Seismological Society of America*. The authors reserve the right to use all or part of the article in future works of their own. In addition, the authors affirm that the article has not been copyrighted and that it is not being submitted for publication elsewhere.

To be signed by at least one of the authors (who agrees to inform the others, if any) or, in the case of "work made for hire," by the employer.



30 September 2017

_____ Print Name (and title, if not author)

_____ Date

PUBLICATION CHARGES

The Seismological Society of America requests that institutions supporting research share in the cost of publicizing the results of that research. The Editor has the discretion of waiving publication charges for authors who do not have institutional support. If pages are paid for by SSA, then no further page charge waivers can be requested for two years by any author listed on the paper. Page charges for waived papers cannot exceed 12 printed pages. Rejected papers in which a page waiver was requested will be considered toward the limit of one request per two years. In addition to regular publication charges there is a nominal fee for publishing electronic supplements, which will not be waived. Current rates are available at <http://www.seismosoc.org/publications/journal-publication-charges/>.

Color options: Color figures can be published (1) in color both in the online journal and in the printed journal, or (2) in color online and gray scale in print. Online color is free; authors will be charged for color in print. You must choose one option for all of the color figures within a paper; that is, you cannot choose option (1) for one color figure and option (2) for another color figure. You cannot submit two versions of the same figure, one for color and one for gray scale. You are responsible for ensuring that color figures are understandable when converted to gray scale, and that text references and captions are appropriate for both online and print versions. Color figures must be submitted before the paper is accepted for publication.

Art guidelines are at <http://www.seismosoc.org/publications/bssa/bssa-art-submission-guidelines/>

Will publication charges be paid? Check one:

YES **BOTH PUBLICATION CHARGES AND COLOR CHARGES WILL BE PAID**, and all color figures for this paper will be color both online and in print. This option requires full payment of publication & color charges.

ONLY PUBLICATION CHARGES WILL BE PAID, and all figures for this paper will be gray scale in print.
Color figures, if any, will be color online.

REQUEST A REDUCTION IN PUBLICATION CHARGES. Send a letter of request and explanation to the Editor-in-Chief at BSSAeditor@seismosoc.org. Color figures, if any, will be color online but gray scale in print.

Send Invoice to: GNS Science, 1 Fairway Drive, Avalon, Lower Hutt, New Zealand

If your paper is accepted for publication, SSA requires that you fill out and submit your final files.

Questions regarding billing should be directed to the SSA Business Office,
400 Evelyn Avenue, Suite 201 Albany, CA 94706 USA Phone 510 525-5474 Fax 510 525-7204